Journal of Materials Chemistry A

ROYAL SOCIETY OF CHEMISTRY

PAPER

View Article Online
View Journal | View Issue

Cite this: J. Mater. Chem. A, 2021, 9, 9882

Optimizing kesterite solar cells from Cu_2ZnSnS_4 to $Cu_2CdGe(S,Se)_4$†

Robert B. Wexler, [a] Gopalakrishnan Sai Gautam ‡[a] and Emily A. Carter *[ab]

Kesterite solar cells, based on the prototypical absorber material Cu_2ZnSnS_4 (CZTS), are cheap, nontoxic, and chemically stable, thus rendering them promising, beyond-Si photovoltaic technologies. Their efficiencies, however, are limited by the formation of defects that decrease the short-circuit current by creating deep traps where nonradiative recombination of photoexcited charge carriers occurs *via* the Shockley–Read–Hall mechanism. To suppress the formation of these defects, specifically the most deleterious $2Cu_{Zn} + Sn_{Zn}$ antisite cluster, we devised an ion substitution strategy involving complete Cd- and Ge-substitution and partial selenization, ultimately arriving at the optimal composition, Cu_2CdGeS_3Se (CCdGSSe). Using density functional theory and *ab initio* thermodynamics, we predict that complete Cd- and Ge-substitution leads to a 125% increase in the formation energy of the deep-trap-inducing $2Cu_{Cd} + Ge_{Cd}$. Additionally, 25% selenization optimizes the predicted band gap (1.43–1.47 eV, as calculated from a hybrid functional) with respect to the Shockley–Queisser limit. In addition to providing a practical and novel ion substitution strategy, we also elucidate the mechanisms of defect suppression and promotion by Ge and Se, highlighting the key role of the inert pair effect and metal-chalcogen bond covalency, respectively. Due to its ideal thermodynamic and electronic characteristics, CCdGSSe should reinvigorate research on kesterite-based solar cells, optimizing the rich materials space afforded by ion substitution and post-quinary compositions.

Received 30th November 2020
Accepted 29th March 2021

DOI: 10.1039/d0ta11603c

rsc.li/materials-a

Introduction

The potential impact of solar energy is unmistakable as it far exceeds global energy needs while simultaneously combating global warming due to its sustainability and carbon-neutrality. To capitalize on this opportunity, the scientific community has spent many decades searching for materials that efficiently convert sunlight to electricity.[1] A number of solar-cell technologies have been commercialized, most notably those based on Si;[2–5] thin-film technologies such as CdTe,[6–8] Cu(In,Ga)Se_2,[9–11] GaAs,[12–14] and hybrid organic–inorganic halide perovskites;[15–17] conductive organic polymers;[18–20] and molecular dyes.[21–23] Although eco-friendly printing techniques have been used to fabricate inexpensive, nontoxic organic/polymer solar cells,[24,25] solar cells with higher efficiency made of promising inorganic materials are as yet unable to supplant fossil-fuel power stations for a number of reasons, including because they contain expensive (Te, In, and Ga) and/or toxic (Cd, Pb, and As) elements or, in the case of perovskite solar cells, have poor resistance to moisture.[26–28] Consequently, solar-energy conversion efficiency, cost, toxicity, ease of production, and stability all must be considered concurrently to design an efficient, scalable, and environmentally friendly solar infrastructure. Over the last decade, there has been growing interest in the solar absorber material Cu_2ZnSnS_4 (CZTS), which contains inexpensive and nontoxic elements, possesses ideal sunlight absorption characteristics (namely, a band gap of ≈1.39–1.52 eV (ref. 29)), and is stable, even in the presence of moisture.[30–33] Unfortunately, under processing conditions (*i.e.*, annealing at 600 K (ref. 34 and 35)), defects can form (*e.g.*, antisites, vacancies, and their clusters), which leads to solar-cell inefficiencies.[36,37]

Two important parameters for optimizing kesterite solar cells are the band gap (E_g) and the concentration of Shockley–Read–Hall (SRH) recombination centers[38,39] (x_{SRH}), as illustrated

[a]Department of Mechanical and Aerospace Engineering, Princeton University, Princeton, NJ 08544-5263, USA. E-mail: eac@princeton.edu

[b]Office of the Chancellor and Department of Chemical and Biomolecular Engineering, University of California, Los Angeles, CA 90095, USA. E-mail: eac@ucla.edu

† Electronic supplementary information (ESI) available: Further details about the effect of Mg- and Si-substitution on CZTS; stability of CCdGSSe against phase separation and decomposition; lowest energy ionic configurations for bulk structures of Ge-substituted CZTS and Cd- and Se-substituted CZGS; polymorph stability for quaternary chalcogenides containing Zn; defect generation protocol; ICSD bulk structures; stability of individual point defects *vs.* clusters; chemical potential limits for CZGSSe and CCdGSSe; lowest energy defect configurations of Ge-substituted CZTS and Cd- and Se-substituted CZGS; effect of Cd- and Se-substitution on the concentration of recombination centers in CZGS; influence of anion order in CCdGSSe on $Cu_{Cd} + Cd_{Cu}$ formation energies; intrinsic stability/instability of CTZS/CZGS-based compounds; experimental band gaps of Cu_2CdGeS_4 and $Cu_2CdGeSe_4$ and predicted defect formation energies for Cu_2CdGeS_3Se and $Cu_2CdGeS_2Se_2$; and formation energy of anion vacancies in CCdGSSe. See DOI: 10.1039/d0ta11603c

‡ Current address: Department of Materials Engineering, Indian Institute of Science, Bengaluru, Karnataka 560012, India.

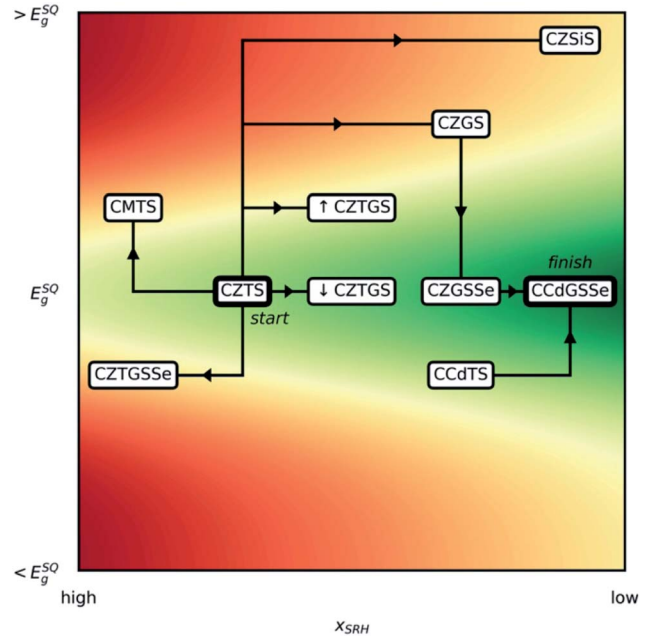

Fig. 1 Schematic road map of substitution strategies considered, from Cu_2ZnSnS_4 (CZTS) to Cu_2CdGeS_3Se (CCdGSSe), where C is Cu^{1+}, Z is Zn^{2+}, M is Mg^{2+}, T is Sn^{4+}, G is Ge^{4+}, ↓CZTGS is $Cu_2ZnSn_{0.875}Ge_{0.125}S_4$, and ↑CZTGS is $Cu_2ZnSn_{0.5}Ge_{0.5}S_4$. The horizontal and vertical axes correspond, respectively, to the concentration of Shockley–Read–Hall recombination centers (x_{SRH})[38,39] and the band gap (E_g), where E_g^{SQ} is the band gap that maximizes the Shockley–Queisser (SQ) limit.[42,43] Red and green contours indicate regions of lower and higher solar cell efficiency, respectively.

in Fig. 1. The band gap of the absorber, which depends on the polymorph ($E_g^{Stannite} < E_g^{Kesterite}$, typically[40,41]), is proportional to the open-circuit voltage (V_{oc}) of the solar cell whereas x_{SRH} is a good measure of the short-circuit current (I_{sc}), with lower concentrations corresponding to higher currents. Given that efficiency is proportional to the product of V_{oc} and I_{sc}, it is clear that increasing I_{sc} by decreasing x_{SRH} increases solar cell efficiency (from high to low x_{SRH}, contours become greener in Fig. 1). The V_{oc}, however, cannot be increased without bound as the Shockley–Queisser limit[42] dictates an optimal E_g of 1.34 eV,[43] with quasi-exponential decline in efficiency upon deviations away from that value.

While in principle CZTS can host a wide range of neutral and charged defects including antisites, vacancies, and their clusters, the effects of the neutral defects listed in Table 1 on the physics and performance of kesterite solar cells are both significant and well-understood. We label defects using a simplified Kröger–Vink notation M_S (in Table 1 and thereafter), where M corresponds to the point defect species, which can be an atom (*e.g.*, Cu) or a vacancy (V), and S indicates the lattice site that the species occupies. For Cu_X + X_{Cu}, Cu^+ and X^{2+} cations swap sites. This leads to the formation of shallow donor (X_{Cu}) and acceptor (Cu_X) levels within the band gap, resulting in spatial fluctuations of the conduction and valence band edges. These fluctuations reduce the effective band gap, thus lowering the V_{oc} of the material.[36,44–49] For Cu vacancies (V_{Cu}), a Cu^+ site is unoccupied, leaving the crystal Cu-deficient. Previous quantum mechanics simulations predicted that Cu vacancies reduce potential fluctuations along the valence band edge, which can mitigate any band gap reduction caused by Cu_X + X_{Cu} clusters.[36] Consequently, V_{Cu} tends to mitigate any reduction in V_{oc}, consistent with the Cu-poor synthesis conditions that typically are employed to achieve highest efficiency.[34,50–52] Finally, for $2Cu_X$ + Y_X, three X^{2+} are replaced by two Cu^+ and one Y^{4+}, leaving the crystal X^{2+}-deficient and Cu^+/Y^{4+}-rich. Previous quantum mechanics studies indicate that $2Cu_{Zn}$ + Sn_{Zn} generates localized trap states near the center of the band gap, which promote SRH recombination and, therefore, reduce the I_{sc} of CZTS.[41,53,54] We note that interface recombination also can reduce the V_{oc},[55,56] however, the goal of the present work was to suppress the formation of bulk defects that are well-known, *via* both experiment and theory, to be detrimental to kesterite solar cell efficiency.

Density functional theory (DFT) and thermodynamic analyses have been employed to improve fundamental understanding of how to control defect formation and to identify promising doping schemes to limit the formation of detrimental defects and improve solar cell performance. For example, theory[57,58] and experiment[59–61] both conclude that Ag-containing phases are more ordered in the 1+ and Zn^{2+} sublattices (*i.e.*, lower concentration of Cu_X + X_{Cu} defects) due to the anisotropic expansion of the unit cell upon replacement of Cu by Ag.[59] Specifically, $Ag_2ZnSnSe_4$ affords a higher predicted maximum photovoltaic efficiency than Cu_2ZnSnS_4,[58] consistent with experiments.[62–70] The alkali metals are another promising group of isovalent replacements for Cu,[62–73] with theory indicating that <25% Na-doping in CZTS suppresses the formation of Cu_{Zn} + Zn_{Cu}.[72] In addition to the Cu^+ site, several studies establish isovalent doping on the Zn^{2+} site as a promising strategy to improve the performance of CZTS-based solar cells as well. Among the 2+ cations considered, which includes the alkaline earth[72,74,75] and transition metals,[57,76–78] Cd has been identified, by both theory[57] and experiment,[77] as one of the most effective at reducing 1+/2+ and 2+/4+ cation disorder. Finally, on the 4+ site, Ge stands out as an exceptional candidate for

Table 1 Defects considered and their effects on the physics of kesterite solar cells and solar cell parameters. X is Zn, Cd, or Mg; Y is Sn, Ge, or Si; E_g is the band gap; V_{oc} is the open-circuit voltage; and I_{sc} is the short-circuit current

Defect	Effect on the physics of kesterite solar cells	Primary effect on solar cell parameters
Cu_X + X_{Cu}	Causes electrostatic potential fluctuations	Decreases V_{oc}
V_{Cu}	Mitigates potential fluctuations along valence band edge	Increases V_{oc}
$2Cu_X$ + Y_X	Causes Shockley–Read–Hall recombination	Decreases I_{sc}

substitution, as numerous studies, mostly experimental, have shown that the combination of partial Ge- and Se-alloying, where the latter serves primarily to optimize the band gap, leads to significant increases in both the V_{oc} and I_{sc} and thus solar-cell efficiency.[58] However, there remains scarce mechanistic understanding of these dopants' influence on defect formation and consequently uncertainty regarding promising directions for improved materials design.

To address this need, here we present predictions of bulk stability, band gap, and formation energies for the key defects in Table 1 and analyze the trends to develop not only a deeper understanding of the quantum mechanical effects that govern defect formation but also a practical strategy for overcoming the efficiency stagnation of kesterite solar-cell technologies over the last six years.[79] To provide a clear picture of the ion substitution strategies we adopted, we first outline the path from CZTS to our newly proposed quinary chalcogenide, Cu_2CdGeS_3Se (CCdGSSe) in Fig. 1. Since CZTS offers a nearly optimal band gap ($\approx$1.5 eV),[80] one would like post-CZTS absorbers to horizontally traverse our schematic road map (Fig. 1). First, we find that Mg- and Si-substitution for Zn and Sn, respectively, increases E_g and, for Mg-substitution, increases x_{SRH} as well, which will lead to inefficient solar cells. Therefore, we do not consider Mg and Si further in the main text (see Tables S1–S3 in Section S1 of the ESI†). Second, we find that complete Ge-substitution (CZGS) decreases x_{SRH} but increases E_g. While partial Ge-substitution (CZTGS) increases E_g by a lesser extent, we find that this approach is not as promising as partial selenization (CZGSSe). Third, inspired by recent studies on Cu_2CdSnS_4 (CCdTS),[57,77] we find that complete Cd-substitution, along with Ge-substitution coupled with partial selenization, provides the optimal band gap and significantly decreases x_{SRH}, thus identifying CCdGSSe as a promising candidate for improving the efficiencies of kesterite-based solar cells. By discussing the steps in our road-map, we reveal both the independent and concerted effects of Ge, Se, and Cd on defect thermodynamics and electronic structure that leads to the optimization of kesterite solar cells, resulting in CCdGSSe.

Computational methods

DFT calculations

We calculated polymorph relative energies, defect formation energies, and band gaps using spin-polarized DFT as implemented in the Vienna *Ab initio* Simulation Package (VASP),[81–83] which employs the projector augmented-wave (PAW) method.[84,85] We used a 520 eV kinetic energy cutoff for the plane wave basis set and initialized atomic magnetic moments of 0.6 μ_B in a ferromagnetic configuration so as not to preclude open shell configurations induced by uncompensated neutral defects, *e.g.*, V_{Cu}, which generates a hole that oxidizes Cu^+, Zn^{2+}, and/or Sn^{4+}. That being said, we find that all final configurations are nonmagnetic. For the calculation of bulk thermodynamic quantities such as polymorph relative energies and defect formation energies, we used both the strongly constrained and appropriately normed (SCAN) meta-generalized-gradient approximation (meta-GGA)[86] and the Heyd–Scuseria–Ernzerhof (HSE) hybrid[87–90] exchange–correlation functionals, where the latter was used to evaluate our most promising candidate, CCdGSSe. For band gap calculations, we used both DFT-HSE and the Perdew–Burke–Ernzerhof (PBE)[91] GGA augmented by a Hubbard U term (PBE+U) where U was derived from unrestricted Hartree–Fock (UHF) calculations[92,93] of binary transition metal (TM) oxide clusters.[94] For PBE+U calculations, we adopted the rotationally invariant approach introduced by Dudarev *et al.*[95] where $U = 3.6$ eV, 4.5 eV, and 4.8 eV were applied on Cu 3d, Zn 3d, and Sn 4d/Ge 3d, respectively.[94] $U = 4.8$ eV was not derived specifically for Ge 3d but the charge state of Sn and Ge should be the same and therefore we used the value derived for Sn here. For Cd-containing compounds, we used DFT-HSE instead of PBE+U despite its significant computational expense since DFT-HSE yields better agreement with experimental band gaps,[96–102] which was needed to evaluate accurately CCdGSSe.

We used the PBE PAW data sets recommended by the Materials Project[103] for Cu ($4s^1\ 5d^{10}$), 2+ cations [Zn ($4s^2\ 3d^{10}$), Mg ($2p^6\ 3s^2$), and Cd ($5s^2\ 4d^{10}$)], 4+ cations [Sn ($5s^2\ 4d^{10}\ 5p^2$), Ge ($4s^2\ 3d^{10}\ 4p^2$), and Si ($3s^2\ 3p^2$)], and 2− anions [S ($3s^2\ 3p^4$) and Se ($4s^2\ 4p^4$)]. Additionally, we applied 0.05 eV of Gaussian electronic smearing to accelerate self-consistent field (SCF) convergence and sampled 32 Γ-point-centered k-points per $Å^{-1}$ to integrate over the Brillouin zone (symmetry was not used to reduce the number of k-points). Fast Fourier transform grids and real space projectors were set using the "accurate" VASP precision mode. All structures were optimized using the conjugate gradient algorithm. For bulk structures we relaxed the lattice constants, angles, and ion positions. For defect structures, however, we optimized the ion positions in a fixed cell corresponding to the predicted equilibrium lattice parameters of the defect-free bulk. For DFT-HSE calculations, due to their computational cost, we used the DFT-SCAN-relaxed geometries followed by a single SCF DFT-HSE calculation. Note that we did not use a SCAN+U framework for any energy evaluation or structure relaxation because we previously found good agreement between DFT-SCAN-predicted and experimental formation enthalpies among binary transition metal sulfides.[57] Finally, we set convergence thresholds of 1×10^{-5} eV for SCF loops and 3×10^{-2} eV $Å^{-1}$ for structure optimization loops.

The ESI† in ref. 104 contains additional details regarding the convergence of bulk thermodynamic quantities with respect to the kinetic energy cutoff, k-point grid density, and the inclusion of semicore states in the PBE PAW data sets for Cu and Ge.

We performed charged defect calculations using the PBE+U+D functional instead of SCAN because the latter grossly underestimates the band gaps of CZTS[57] and CZGS.[104] Further details about the phonon calculations to evaluate the thermodynamic stability of CCdGSSe can be found in Fig. S1–S3 and Table S4 in Section S2 of the ESI.†

Structural models

Polymorph structures. Prior to defect formation energy calculations, we determined the lowest energy crystal structure

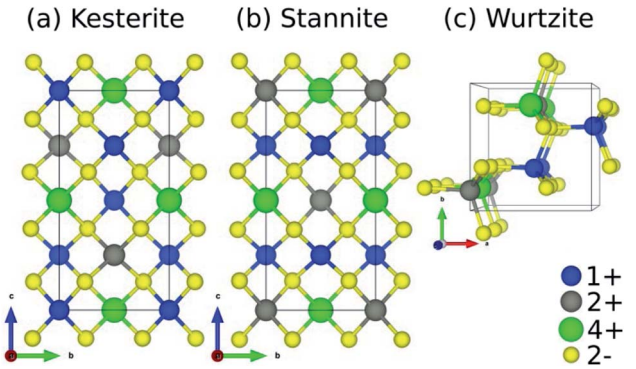

Fig. 2 Crystal structures of quaternary chalcogenides adopting the (a) kesterite, (b) stannite, and (c) wurtzite polymorphs. The prototypical composition for kesterite solar cells is Cu_2ZnSnS_4 where Cu^{1+}, Zn^{2+}, Sn^{4+}, and S^{2-} occupy the 1+ (blue spheres), 2+ (grey), 4+ (green), and 2− (yellow) sites, respectively.

of the defect-free material. CZTS-like quaternary chalcogenides typically exist in one of three polymorphs: kesterite, stannite, and wurtzite-stannite (which, for simplicity, we will refer to as wurtzite),[80] which are displayed in Fig. 2. All three polymorphs comprise corner-sharing tetrahedrons of four-fold anion-coordinated 1+, 2+, and 4+ cations. The kesterite and stannite polymorphs have similar space groups ($I\bar{4}$ and $I\bar{4}2m$, respectively) but differ in terms of their cation layer composition along c, where kesterite has alternating 1+/2+ and 1+/4+ layers and stannite has alternating 1+ and 2+/4+ layers. The main difference between wurtzite (space group: $P6_3mc$) and kesterite/stannite is the underlying S-arrangement.

Bulk structures. For (partial) ion-substituted CZTS, we also determined the lowest energy ionic configuration. In the case of Ge-substituted CZTS, we considered both the kesterite and stannite polymorphs and two concentrations of Ge: dilute (x_{Ge} = Ge/(Sn + Ge) = 0.0625) and high (x_{Ge} = 0.5). For dilute Ge, which we refer to as ↓CZTGS, there is only one possible symmetry-unique Sn/Ge configuration within a 2 × 2 × 2 supercell, *i.e.*, Ge in the Cu/Sn layer of kesterite and the Zn/Sn layer of stannite (see Fig. S4 in Section S3.1.1 of the ESI†). Note that, in order to calculate defect formation energies at infinite Ge dilution, we fixed the cell to that of relaxed CZTS. For all other bulk structures considered, we relaxed the lattice vectors and ions. For high Ge-substitution, which we refer to as ↑CZTGS, we optimize the cell and, to reduce the number of Sn/Ge configurations, we only used the one possible symmetry-unique Sn/Ge configuration in the 16-atom conventional cell (see Fig. S5 in Section S3.1.2 of the ESI†).

For Se-substituted CZGS (*i.e.*, CZGSSe), we considered all symmetry-unique S/Se configurations for x_{Se} = Se/(S + Se) = 0.5 in the 16-atom conventional cell of kesterite and stannite CZGS. We used pymatgen's[105] structure matcher, which is powered by spglib,[106] to generate the symmetry-unique configurations of which there are 12 for kesterite and 10 for stannite (see Fig. S6 in Section S3.2 of the ESI†). Finally, for CCdGSSe, in the same way as for CZGSSe, we considered all symmetry-unique S/Se configurations for x_{Se} = 0.25 in kesterite (there are five), stannite (five), and wurtzite (11) Cu_2CdGeS_4 (CCdGS; see Fig. S7 in Section S3.3 of the ESI†). We included the wurtzite polymorph for CCdGSSe because it is observed experimentally for CCdGS[107] and CCdGSe[108] and it is nearly isoenergetic with stannite. Wurtzite is not relevant, however, for the quaternary chalcogenides containing Zn (CZTS, CZGS, CZTSe, or CZGSe) because it is less stable than the kesterite (ground state) and stannite (metastable) phases (see Table S5 in Section S4 of the ESI†).

Defect structures. All defects were generated in 2 × 2 × 2 supercells of their defect-free, bulk kesterite, stannite, or wurtzite structures (consistent with previous studies[57,72,77]) using the protocol described in Table S6 in Section S5 of the ESI.† The objective of this study was to identify strategies, specifically those involving ion substitution, for the suppression of $Cu_X + X_{Cu}$ and $2Cu_X + Y_X$ and the promotion of V_{Cu}. Y in this paper refers strictly to either Ge or Sn and does not refer to the element Yttrium. To this end, we primarily focused on ion substitution at the 2+ and 4+ sites as these are directly involved in the defects we were trying to suppress and have not yet been studied exhaustively. As shown in Fig. 3, we considered Zn, Mg, and Cd at the 2+ site; Sn, Ge, and Si at the 4+ site; and S and Se at the 2− site. These selections were the result of discarding elements that are radioactive (green), rare (gold), redox-active (magenta), possess the wrong oxidation state (*i.e.*, not 2+, 4+, or 2−), or too small/large in terms of their ionic radius (blue) (see Fig. 3 caption for ionic radius filtering criteria). We did not

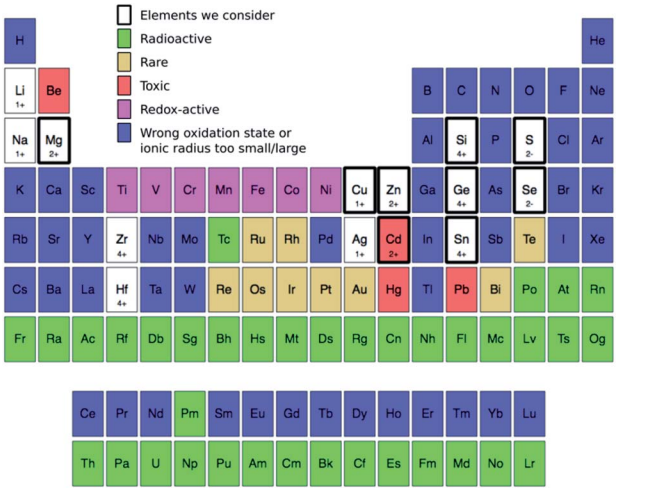

Fig. 3 Elements we consider in this study (thick black rectangles) to occupy the 1+, 2+, 4+, and 2− sites in Fig. 2: Cu (1+), Zn (2+), Cd (2+), Mg (2+), Sn (4+), Ge (4+), Si (4+), S (2−), and Se (2−). We filter these elements from the known 118 by removing, in the following order, those that are radioactive[168] (green), rare (gold),[132] redox-active (magenta), have either the wrong oxidation state or whose ionic radius is too different (blue). For ionic radius, we eliminate all elements that are too small (*i.e.*, <30%) or too large (>170%) compared to the ionic radius of four-fold-coordinated Cu^{1+}, Zn^{2+}, Sn^{4+}, and S^{2-} corresponding to the occupation of 1+, 2+, 4+, and 2− sites, respectively.[149] While the use of toxic elements (red) should be restricted,[169] we retain them under consideration. For the remaining elements, we provide their most likely oxidation state in the prototype kesterite structure (Fig. 2a), *e.g.*, Ge is 4+ and Se is 2−.

consider redox-active elements because they can promote defect formation, *e.g.*, Mn can occupy both the 2+ and 4+ sites thereby promoting 2+/4+ disorder. We also did not consider Li^+ and Zr^{4+} because Li_2ZnSnS_4 and $Cu_2ZnZrSe_4$ are wide-band-gap semiconductors (2.87 eV (ref. 109) and 1.95 eV,[110] respectively); Ag^+, Na^+, and Ti^{4+} because Ag- and Na-substituted CZTS, and $Cu_2ZnTi(S,Se)_4$ already have been studied computationally[57,72,111] and experimentally;[60,67,78,112] and Hf^{4+} because there is scarce experimental evidence of Hf forming quaternary chalcogenides (such as $Cu_2ZnHf(S/Se)_4$). We considered toxic elements (red) like Cd because toxicity can be mitigated through the practice of thoughtful device engineering.[113] For example, previous efforts have successfully devised encapsulation schemes to ensure that CdTe solar cells, which contain more Cd by mass (47 wt%) than CCdGSSe (23 wt%), are significantly less toxic than they ought to be.[114–116] Hence, depending on how sensitive to moisture and air CCdGSSe is in practice, similar encapsulation and water-proofing schemes will be useful for large-scale deployment. In contrast to toxicity, abundance, oxidation state, and ionic radius are, to a large extent, immutable characteristics and the effects of radioactivity are difficult to contain.

Ab initio thermodynamics

Convex hull construction. To determine the chemical potentials at which the quaternary chalcogenides (CZTS, CZGS, CZGSe, CCdGS, and CCdGSe) are in equilibrium with different combinations of secondary phases containing their constituent ions, we constructed 0 K phase diagrams using pymatgen,[105] which takes as inputs the DFT-SCAN (or DFT-HSE for CCdGSSe) total energies of all sub-quinary compounds and elements. Bulk structures for elements, binaries, ternaries, and quaternaries containing Cu, Zn, Mg, Cd, Sn, Ge, Si, S, and Se were taken from the inorganic crystal structure database (ICSD,[117] see Table S7 in Section S6 of the ESI†). We relaxed these structures with DFT-SCAN and used the same PAW potentials, kinetic energy cutoff, and *k*-point sampling density as above. Our previous work showed that DFT-SCAN systematically underestimates the formation energies of Ge-containing compounds by 0.27 eV/Ge.[104] Therefore, we subtract 0.27 eV/Ge from all DFT-SCAN formation energies of Ge-containing compounds.

Defect formation energies. In the screening part of this study, we considered only neutral defects, meaning that atoms are removed from or added to the structure in their neutral elemental form. Once we identified an optimal composition, we then characterized charged defects for that composition. Our reasons for this more efficient screening approach were four-fold. (1) Charged-defect calculations are used primarily to identify defect transition energy levels within the band gap and to indicate their type (*i.e.*, shallow or deep) and their influence on the majority charge carrier concentrations. (2) Previous studies already reported the defect transition energy levels for Cu_X, X_{Cu}, V_{Cu}, and Y_X (*i.e.*, the main antisites we considered), and showed that (a) charged Cu_X, X_{Cu} and V_{Cu} defects produce shallow gap states that do not significantly promote nonradiative recombination[36,41,57] and (b) while charged Y_X defects do produce trap states,[41,53] their depth does not depend strongly on the identity of Y.[58] On the other hand, the depth of Y_X charged defect transition levels does depend on the identity of X (*vide infra*). For X = Zn, ref. 58 shows that Y_{Zn} defects produce trap states within the band gap of CZTS. We therefore did examine X = Cd within our optimal composition case. Our results (right panel of Fig. 8) show that Ge_{Cd} exhibits deep donor levels, which lie within the valence band, resulting in Ge_{Cd} exhibiting a neutral charge state across the band gap. Thus, we do not expect the donor transition levels of Ge_{Cd} to act as electron traps in CCdGSSe. (3) We consider antisite clusters that are locally charge-balanced (*e.g.*, the electron-deficient Cu_X compensates the electron-excessive X_{Cu} adjacent to it in $Cu_X + X_{Cu}$); non-charge-balanced defect clusters generally are less stable than charge-balanced ones (see Table S8 and Fig. S8 in Section S7 of the ESI†). For materials other than our newly proposed CCdGSSe, the only charge-imbalanced defect we consider is V_{Cu}, whose charged formation energies were studied previously.[41,50] Like Y_X in CZTSe, CZTS, and CZGSe, however, the depth of its transition energy level does not depend strongly on the identity of the 2+, 4+, and 2− ions; only upon complete Ag-substitution in CZTSe (which is not considered here) does the transition energy level change.[58] Additionally, since its transition energy level is shallow, increasing the Fermi level stabilizes V_{Cu}, which increases the majority charge carrier (*i.e.*, hole) concentration and V_{oc}.[36] (4) Neutral defect formation energies are better metrics for estimating intrinsic defect concentrations than those of charged defects because the latter depend strongly on the Fermi level, which can be influenced by external conditions. Indeed, a recent experimental study on the photoluminescence of CCdGS[118] indicate that the material has minimal carrier traps that lie deep within the band gap, which is in qualitative agreement with our neutral defect formation energy calculations.

Neutral defect formation energies were calculated as

$$\Delta E_f^d = E_d^{SCAN} - E_b^{SCAN} + \sum_i n_i \mu_i \quad (1)$$

where d is the defect supercell, b is the bulk supercell, n is the number of neutral atoms removed from ($n > 0$) or added to ($n < 0$) the system to form defect d, i is an index that runs over the unique species in the compound, and μ is the corresponding chemical potential. When point defects are created, the atoms that contribute to forming such defects must be exchanged with an external reservoir. Experimentally, this external reservoir may be ambient atmosphere during annealing, the current collecting phases that are in contact, or a secondary phase, such as leftover binary phases (*e.g.*, CdS) that were used for the actual synthesis of the chalcogenide absorber. While theoretically we can calculate the formation energies of various isolated defects and defect complexes over a range of thermodynamically possible chemical potentials, the specific experimental conditions will precisely define the formation energy of a given defect. Here, we adopt the Cu-poor experimental conditions,[57] with the phases that coexist with the quaternary/quinary chalcogenide determined by the 0 K phase diagram (*i.e.*, convex hull) of the overall quaternary/quinary system. We selected Cu-poor chemical potential limits for CZGSSe and CCdGSSe because CZTS and CCdTS

synthesized under this condition achieve high efficiency.[34,50–52,77] For example, under Cu-poor conditions, CZTS is in equilibrium with ZnS, SnS_2, and S; CZGS is in equilibrium with ZnS, GeS_2, and S; and CZGSe is in equilibrium with ZnSe, $GeSe_2$, and Se. CZTGS, CZGSSe, and CCdGSSe are metastable compounds at 0 K with the equilibrium compounds at their compositions being CZTS, CZGS, ZnS, SnS_2, and S; CZGS, ZnS, GeS_2, S, and Se; and CCdGS, Cd_4GeS_6, GeS_2, S, and Se, respectively. For metastable compounds, we use the chemical potentials determined by the stable compounds (see Table S9 in Section S8 of the ESI†). We did not consider the effect of temperature on the variation of chemical potentials in our calculations but we expect this effect to be small between 0 K and 298 K. For additional details on the computational methods, please see the ESI† and ref. 104, from which the DFT calculations performed herein are based.

For completeness, we did consider the following charged defects and defect clusters to examine the possible role of defect transition levels in our newly proposed CCdGSSe: Cu_{Cd} ($q = -1$, 0, 1), Cd_{Cu} ($q = -1, 0, 1$), Ge_{Cd} ($q = -1, 0, 1, 2$), V_{Cu} ($q = -1, 0, 1$), V_S ($q = -1, 0, 1, 2$), V_{Se} ($q = -1, 0, 1, 2$), $V_S + Cu_{Cd}$ ($q = -1, 0, 1$), $V_{Se} + Cu_{Cd}$ ($q = -1, 0, 1$), and $Ge_{Cd} + Cu_{Cd}$ ($q = -1, 0, 1$). Charged defect (cd) formation energies were calculated as $\Delta E_f^{cd} = \Delta E_f^{d} + qE_F + E_c$ where E_F is the Fermi energy of the pristine bulk structure and E_c is the electrostatic correction term, calculated using the correction scheme of Kumagai and Oba[119] as implemented in the Spinney package.[120] For further details about the correction scheme, we refer the interested reader to ref. 57, as we used the same approach here. The PBE+U dielectric tensor of CCdGSSe used in our charge defect calculations is: $\varepsilon_{xx} = \varepsilon_{yy} = 10.5$, $\varepsilon_{zz} = 9.97$, $\varepsilon_{xy} = \varepsilon_{yz} = -0.06$, and $\varepsilon_{zx} = 0.06$.

Results

Effect of Ge-substitution in CZTS

Given the deep-trap-inducing nature of $2Cu_{Zn} + Sn_{Zn}$ antisite clusters in CZTS[53] and the primary role played by the Sn_{Zn} antisite,[41] we first explore the replacement of Sn^{4+} with varying amounts of Ge^{4+}. Fig. 4 shows the effect of dilute (light blue), high (dark blue), and complete (purple) Ge-substitution in CZTS (green) on kesterite *vs.* stannite polymorph preference (panel a), neutral defect formation energies under experimentally relevant Cu-poor conditions (panel b), and the PBE+U band gap (panel c). First, our results show that Ge-substitution does not affect polymorph preference (panel a) with kesterite being the ground-state polymorph ($E_{Stannite} - E_{Kesterite} > 0$ eV per formula unit) for all x_{Ge} (see Table S5 in Section S4 of the ESI† for CZTS and CZGS wurtzite data). That Ge increases the relative stability of kesterite *vs.* stannite for all but dilute Ge-substitution is in general agreement with other theoretical work[59,121,122] and the experimental observation of enhanced grain growth in Ge-doped CZTSSe.[123–125] Recent scanning electron microscope images show that grain growth and crystallinity in CZTGS is not improved for $x_{Ge} > 0.2$[121] but this could be due to suboptimal annealing conditions for each Ge composition during fabrication.[107,126,127] Accordingly, non-dilute Ge-substitution should favor kesterite formation and suppress E_g/V_{oc} lowering due to the kesterite → stannite phase transition.[80]

Next, we analyze trends in defect formation energies as a function of x_{Ge} (panel b). For the $Cu_{Zn} + Zn_{Cu}$ antisite clusters, we find that, while partial Ge-substitution does not influence their formation (0.22 eV for CZTS[57] and ~0.23 eV for both ↓CZTGS and ↑CZTGS), complete substitution has a promoting effect (0.15 eV for CZGS), which can be explained by the greater

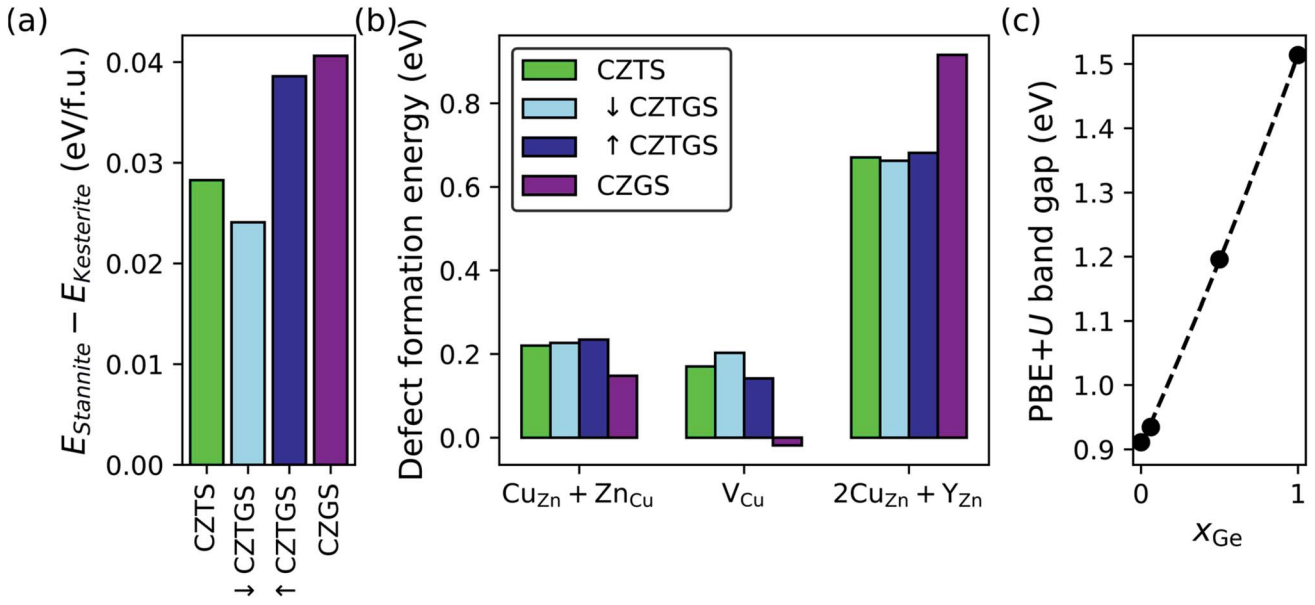

Fig. 4 Effect of Ge-substitution on (a) the DFT-SCAN relative stability of the stannite and kesterite polymorphs, (b) DFT-SCAN defect formation energies under Cu-poor conditions, and (c) the PBE+U band gap. In (b) Y is either Sn or Ge, whichever gives the lower defect formation energy; Y is Sn for CZTS, ↓CZTGS, and ↑CZTGS; and Ge for CZGS. (c) x_{Ge} is Ge/(Sn + Ge). Minimum energy defect configurations can be found in Fig. S9–S11 in Section S9.1 of the ESI.†

covalency of Ge–S bonds (ΔEN = 0.57, where EN is the Pauling electronegativity) compared to Sn–S bonds (ΔEN = 0.62). Ge–S bond covalency, which is greatest for complete Ge-substitution, reduces the charge density on S and promotes covalency across the Cu–S and Zn–S bonds. In turn, higher covalency reduces the effective 1+ and 2+ charges on the Cu and Zn, respectively, and consequently, the electrostatic energy penalty for Cu_{Zn} + Zn_{Cu} disorder. Therefore, CZGS should be more susceptible to Cu/Zn-disorder-induced potential fluctuations, as is seen in ref. 59, and potential V_{oc} deficit. Several studies found that partial Ge-substitution in CZTSSe increases the V_{oc},[124,128–131] however, we emphasize that these materials are selenized and, as we will explain in the next section, selenization suppresses stannite and promotes V_{Cu} in CZGS.

For Cu vacancies, with the exception of ↓CZTGS (0.20 eV), we predict that Ge-substitution decreases their formation energy (0.17 eV for CZTS,[57] 0.14 eV for ↑CZTGS, and −0.02 eV for CZGS) to the extent that DFT-SCAN predicts a nonzero equilibrium concentration of V_{Cu} in CZGS at 0 K. In all likelihood, this negative value for V_{Cu} in CZGS is an artifact of DFT-SCAN's tendency to produce lower values of ΔE_f^d compared to DFT-PBE, PBE+*U*, SCAN+*U*, and DFT-HSE.[104] For example, compared to DFT-HSE, DFT-SCAN predicts the ΔE_f^d for V_{Cu} to be lower by 0.53 eV in CZTS[104] and 0.58 eV in CZGS. Importantly, qualitative trends in ΔE_f^d are XC-functional-insensitive (see Fig. S5 in the ESI† for ref. 104) and we therefore simply interpret this negative value as "high to complete Ge-substitution promotes V_{Cu} formation".

The decrease in the V_{Cu} formation energy upon complete replacement of Sn with Ge can be rationalized as follows. The Ge–S 298 K neutral diatomic bond dissociation enthalpy (BDE = 5.54 ± 0.03 eV) is substantially larger than that of Sn–S (4.84 eV)[132] and, by replacing Sn–S bonds with stronger Ge–S bonds, Ge-substitution effectively weakens Cu–S bonds. As a result, less energy is required for Cu to break its bonds with S and form vacancies. In terms of solar cell parameters, the low ΔE_f^d for V_{Cu} in CZGS should mitigate the V_{oc}-lowering effects associated with complete Ge-substitution.

Finally, for $2Cu_{Zn}$ + Y_{Zn} antisite clusters, where Y is either Sn or Ge, it is clear that complete Ge-substitution strongly suppresses their formation (0.92 eV) compared to CZTS (0.67 eV), ↓CZTGS (0.66 eV), and ↑CZTGS (0.68 eV). The difference between CZTS and CZGS (0.25 eV) can be attributed to the inert pair effect, which stabilizes the 2+ oxidation state of Sn and, therefore, stabilizes Sn on the Zn^{2+} site by reducing it from 4+ to 2+. Ge, on the other hand, only exists stably in a 4+ oxidation state, as evidenced by the positive ΔG_{298} for the reduction of GeS_2 to GeS (0.80 eV), *i.e.*, $Ge(IV)S_2 \rightarrow Ge(II)S + S$.[133] Furthermore, Ge-substitution suppresses $2Cu_{Zn}$ + Y_{Zn} only under complete substitution because Ge does not affect the $2Cu_{Zn}$ + Sn_{Zn} formation energies and these defect clusters will continue to form as long as Sn, which is susceptible to reduction *via* the inert pair effect, is present in the structure. Hence, unless the more redox active Sn is completely replaced by the less redox active Ge, the ΔE_f^d for $2Cu_{Zn}$ + Y_{Zn} should remain close to that for CZTS. With that being said, partial Ge-substitution still can suppress the formation of $2Cu_{Zn}$ + Y_{Zn} by reducing x_{Sn}, thus shedding light on the experimentally observed increase in minority charge carrier lifetimes for Ge-alloyed (x_{Ge} = 0.3) CZTSSe.[130]

Via its substantial suppression of $2Cu_{Zn}$ + Y_{Zn}, as compared to other strategies in the literature,[77] CZGS should offer a significant reduction in the rate of SRH recombination *vs.* CZTS. Unfortunately, despite the promising defect thermodynamics of CZGS, the band gap depends strongly on x_{Ge} (panel c) with a quasi-linear increase from CZTS (0.91 eV for PBE+*U* and ≈1.5 eV in experiments[80]) to CZGS (1.51 eV for PBE+*U* and ≈2.1 eV in experiments[134]). In summary, while only CZGS suppresses $2Cu_{Zn}$ + Y_{Zn} (rightward trajectory in Fig. 1), its E_g is well above E_g^{SQ} (upward trajectory), thus prompting our next ion substitution strategy.

Effect of selenization on CZGS

One way to reduce the band gap of CZGS is Se-substitution (also known as selenization);[134–138] this has been used extensively to reduce/optimize the band gap of CZTS.[139,140] Band gap reduction in both CZTS and CZGS upon selenization can be explained by the slightly lower electronegativity of Se (2.55 on the Pauling scale[141,142]) compared to S (2.58), which pushes the valence band edge (comprising mostly Cu 3d and anion p states) up in energy but does not affect the conduction band edge (mostly Sn 5s).[139] As a result, the band gap shrinks and the extent to which it does depends on x_{Se} = Se/(S + Se). In Fig. 5, we consider both 50% (light green bars) and 100% (cyan bars) selenization (CZGSSe and CZGSe, respectively) in CZGS (yellow bars). Fig. 5a shows that the crystal structure of the lowest energy S/Se configuration of kesterite CZGSSe (see Section S3.2 in the ESI†) is composed of alternating S and Se (011) planes (red lines). As expected, our results show that selenization decreases E_g^{PBE+U} (panel b) from 1.51 eV (CZGS) to 0.59 eV (CZGSe), with the magnitude of the decrease in excellent agreement with the experimental[134,137,138] and theoretical literature.[135] Additionally, we find that the PBE+*U* band gap of CZGSSe (0.92 eV) is approximately equal to the optimal CZTS value (black dotted line at 0.91 eV). With respect to polymorph preference, the introduction of 50% Se (CZGSSe) marginally stabilizes the low-E_g stannite polymorph (green, panel c) relative to CZGS (yellow) but not with respect to CZTS (black dotted line), thus signaling that selenization should not exacerbate polymorphism-derived V_{oc} deficits.

In view of the favorable band gap and stability of kesterite CZGSSe, we investigate the dependence of defect formation energies on x_{Se} (panel d). First, we find, as do powder neutron diffraction measurements,[59] that selenization slightly suppresses the formation of V_{oc}-reducing Cu_{Zn} + Zn_{Cu} antisite clusters relative to CZGS (0.15 eV for CZGS *versus* 0.20 and 0.16 eV for CZGSSe and CZGSe, respectively; CZTS is 0.22 eV). Furthermore, we predict that selenization promotes E_g-increasing/V_{oc}-restoring Cu vacancies (−0.02 eV for CZGS *versus* −0.12 and −0.09 eV for CZGSSe and CZGSe, respectively), due to the decrease in bond strength from Cu–S (BDE = 2.85 ± 0.15 eV) to Cu–Se (2.64 ± 0.15 eV)[132] and the endoergicity of $Cu_2S + Se \rightarrow Cu_2Se + S$ (ΔG_{298} = 0.12 eV). In spite of these promising trends, selenization counteracts the Ge-induced suppression of I_{sc}-

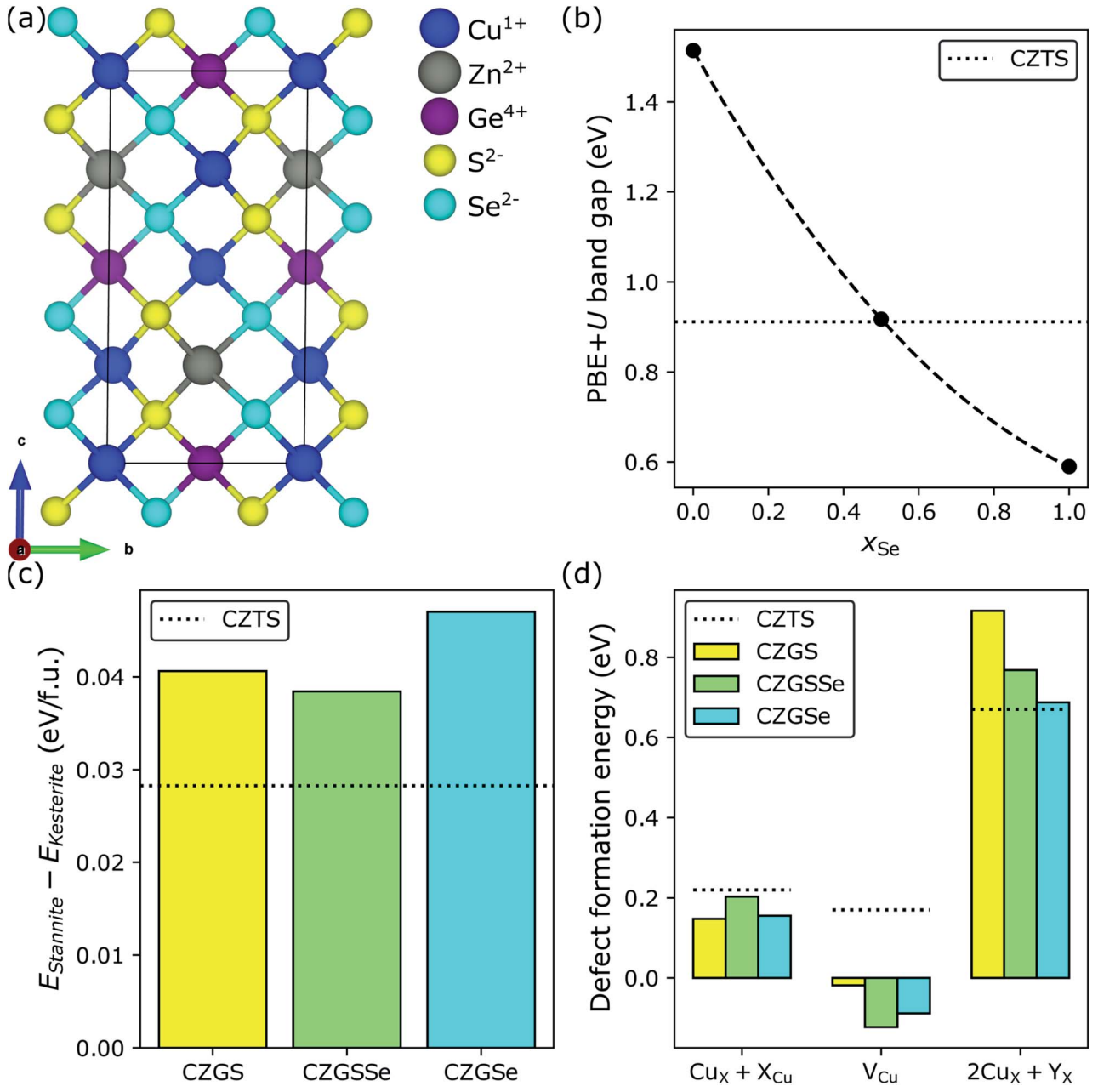

Fig. 5 Selenization of CZGS. (a) Crystal structure of the minimum-energy configuration of $Cu_2ZnGeS_2Se_2$ (CZGSSe), where the anion ordering is similar to how cations order in $CuIn(S,Se)_2$. Effect of selenization on (b) the PBE+U band gap, (c) the DFT-SCAN relative stability of the stannite and kesterite polymorphs, and (d) DFT-SCAN defect formation energies under Cu-poor conditions. Minimum-energy defect configurations can be found in Fig. S12 and S13 in Section S9.2 of the ESI.†

lowering $2Cu_{Zn} + Ge_{Zn}$ antisite clusters (0.92 eV for CZGS > 0.77 eV for CZGSSe > 0.69 eV for CZGSe ≈ 0.67 eV for CZTS, black dotted line). We ascribe this phenomenon to the following mechanism. While $2Cu_{Zn} + Ge_{Zn}$ is charge-balanced, the balancing charges (two holes and two electrons from $2Cu_{Zn}$ and Ge_{Zn}, respectively) are slightly delocalized.[104] Therefore, it is reasonable to expect that the stability of $2Cu_{Zn} + Ge_{Zn}$ depends, to some extent, on the anion's tolerance for delocalization. Since Se is less electronegative (and more polarizable) than S, it should be able to accommodate more delocalization and, therefore, stabilize $2Cu_{Zn} + Ge_{Zn}$. Thus, selenization of CZGS should decrease I_{sc}, counteracting the beneficial suppression of $Cu_{Zn} + Zn_{Cu}$ and promotion of V_{Cu}. A final ion substitution step therefore must be taken in order to minimize the need for E_g-remediating but I_{sc}-decreasing selenization in CZGS.

Cooperative effect of Cd-substitution and selenization on CZGS

Recently, it was predicted and subsequently observed that replacing the Zn in CZTS with Cd, under Cu-poor conditions,

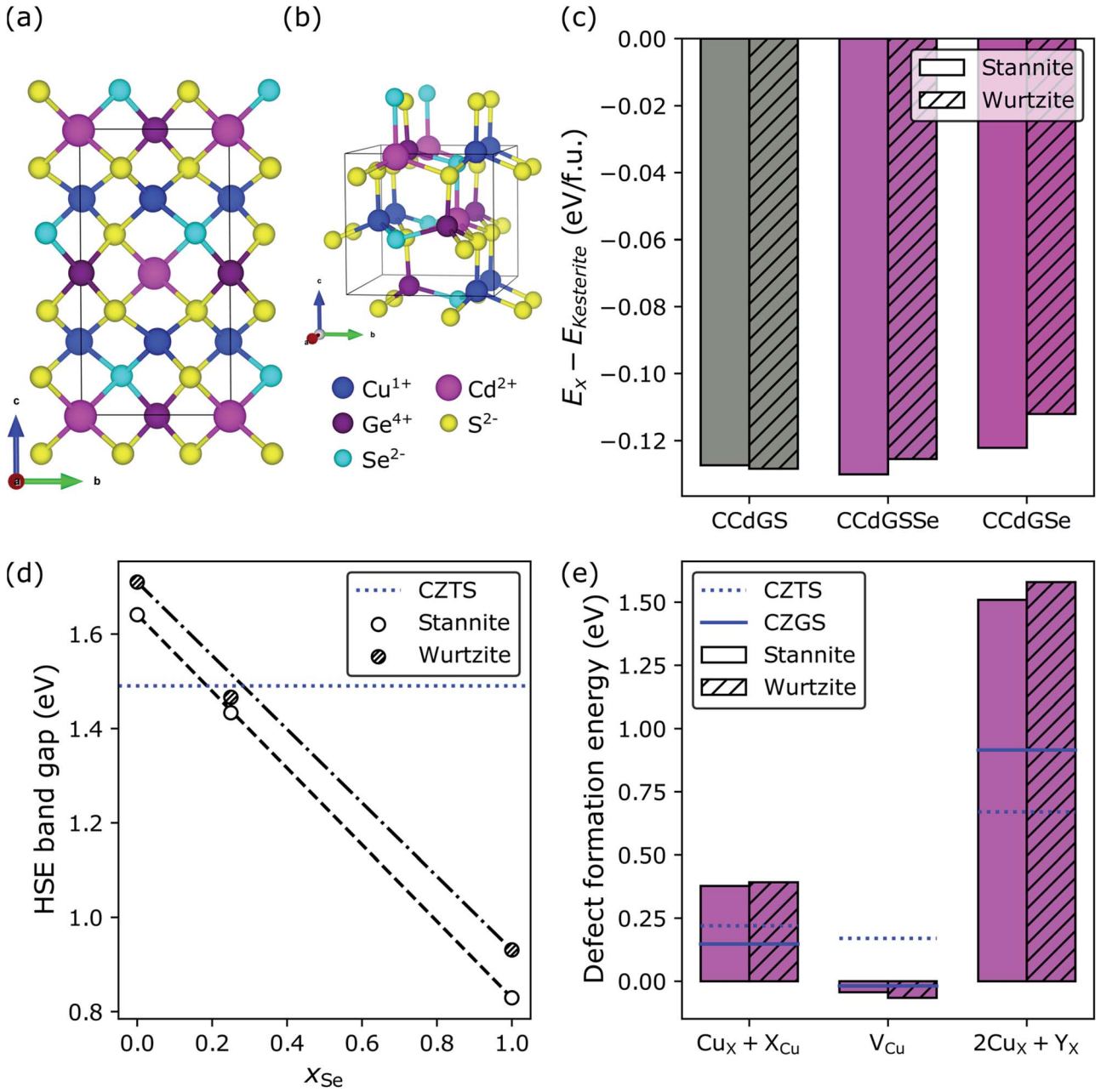

Fig. 6 Cd-substitution and selenization of CZGS. Crystal structures of the minimum-energy configurations of the (a) stannite and (b) wurtzite polymorphs of Cu_2CdGeS_3Se (CCdGSSe). Effect of Cd-substitution and selenization on (c) the DFT-HSE relative stabilities of the stannite, wurtzite, and kesterite polymorphs, (d) the DFT-HSE band gap (CZTS value is from ref. 143 while the other band gaps were calculated by us), and (e) DFT-SCAN defect formation energies under Cu-poor conditions for CCdGSSe. Minimum-energy defect configurations can be found in Fig. S14 and S15 in Section S9.3 of the ESI.†

decreases its band gap and suppresses the formation of the deep-trap-level-inducing $2Cu_X + Sn_X$, where X is either Zn or Cd.[57,77] For these reasons, Cd-substitution in CZGS should limit the extent to which selenization is necessary and further suppress the formation of I_{sc}-lowering defects. To test this hypothesis, in Fig. 6, we consider complete Cd-substitution in CZGS, leading to CCdGS (grey bars), and with 25% (purple bars) and 100% selenization (magenta bars), where the former was chosen as an intermediate Se-substitution condition by interpolating between the DFT-HSE band gaps of CCdGS and CCdGSe to find the value of x_{Se} for which E_g^{HSE}[CCdGSSe] ≈ E_g^{HSE}[CZTS] = 1.49 eV.[143,144] Fig. 6a and b show the ground state S/Se configuration in stannite and wurtzite CCdGSSe, respectively (see Section S3.3 in the ESI†). In what follows, we examine both of these polymorphs because they are nearly isoenergetic (panel c) and more stable than kesterite ($E_x - E_{Kesterite} < 0$). Fortunately, the DFT-HSE band gaps of stannite and wurtzite CCdGSSe are similar in terms of their dependence on x_{Se} (panel

d) and achieve optimality at 25% selenization (1.43 and 1.47 eV for stannite and wurtzite, respectively), which suggests that, despite the polymorphism that is likely present in real samples, the energy offset between bands at stannite–wurtzite interfaces and, therefore, interfacial recombination rates[145–148] should be small. Furthermore, optimality at $x_{Se} = 0.25$ indicates that complete Cd-substitution cuts the need for Se-substitution in half, compared to CZGS → CZGSSe.

Perhaps the most dramatic effect of Cd-substitution is on the defect thermodynamics of CZG(S,Se). Fig. 6e reveals that Cd-substitution suppresses the formation of V_{oc}-lowering $Cu_{Cd} + Cd_{Cu}$ antisite clusters in CCdGSSe (0.38 eV and 0.39 eV for stannite and wurtzite, respectively) compared to $Cu_{Zn} + Zn_{Cu}$ in CZTS (blue dotted line at 0.22 eV) and more than doubles the $Cu_{Zn} + Zn_{Cu}$ ΔE_f^d in CZGS (blue solid line at 0.15 eV). The suppression of $Cu_X + X_{Cu}$ can be attributed to the larger ionic radius of Cd^{2+} compared to Cu^+ and Zn^{2+}.[149] Additionally, Cd-substitution promotes the formation of V_{oc}-increasing Cu vacancies (−0.04 eV and −0.07 eV for stannite and wurtzite, respectively) compared to CZTS (0.17 eV), while the ΔE_f^d for V_{Cu} in CCdGSSe is quite similar to CZGS (−0.02 eV). Thus, the stronger Ge–S bonds (*versus* Sn–S bonds) primarily govern the ease of formation of V_{Cu} in Ge-containing quaternary/quinary chalcogenides. Most importantly, Cd-substitution leads to a remarkably strong suppression of $2Cu_{Cd} + Ge_{Cd}$ in CCdGSSe (1.51 and 1.58 eV in stannite and wurtzite, respectively) relative to CZTS (0.67 eV) and CZGS (0.92 eV). The much higher ΔE_f^d corresponds to a roughly seven orders of magnitude decrease in x_{SRH} (see Section S10 in the ESI†) under CZTS annealing conditions (600 K),[34,35] *i.e.*, the maximum temperature to which CZTS is heated during synthesis, thus constituting an upper bound for crystalline defect concentrations. The significant suppression of $2Cu_{Cd} + Ge_{Cd}$ can be attributed to the large ionic radius difference between Cd^{2+} (0.78 Å in tetrahedral coordination) and Ge^{4+} (0.39 Å).[149] Note that the local anionic configuration of CCdGSSe does not affect significantly its defect formation energies ($\sigma_{\Delta E_f^d} = 0.06$ eV, see Fig. S16 and Table S10 in Section S11 of the ESI†).

To the best of our knowledge, there are neither reports on the synthesis of CCdGSSe (no entries in both the ICSD and Chemical Abstracts Service), experimental/computational characterizations of its solar cell parameters (E_g/V_{oc}, I_{sc}, and FF), nor publications/patents detailing the fabrication of CCdGSSe-based solar cells. Therefore, CCdGSSe may provide the innovation necessary to improve the efficiency of kesterite-inspired solar cells beyond their 12.6% efficiency record for CZTSSe[79] that has remained stationary since 2013, and propel them toward competitiveness[150] with Si (26.7%)[3] and hybrid perovskites (25.2%).[151]

Discussion

Having discussed Ge-, Se-, and Cd-substitution individually (in order to reveal their independent effects on defect thermodynamics and electronic structure), we now, in Fig. 7, compare the performance of CZTS (green), CZGS (red), CZGSSe (blue), and CCdGSSe (magenta). The origin, *i.e.*, (0,0,0), is the center of the

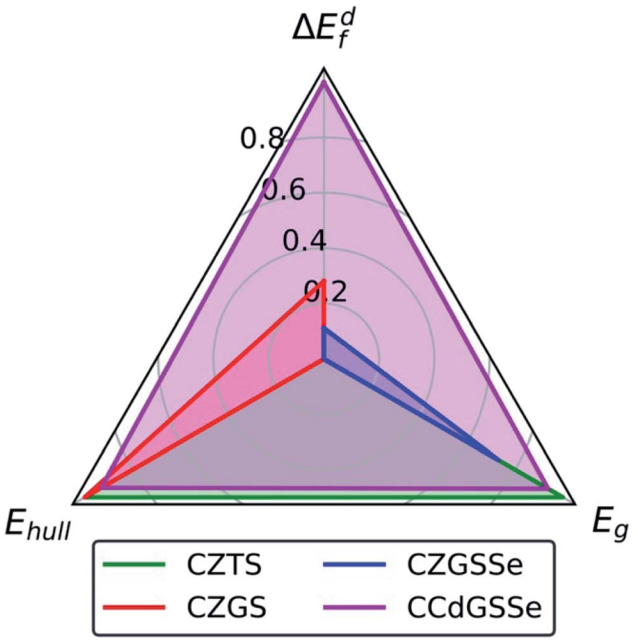

Fig. 7 Variation in performance among CZTS, CZGS, CZGSSe, and CCdGSSe where ΔE_f^d is the normalized $2Cu_X + Y_X$ formation energy under Cu-poor conditions, E_{hull} is the energy/atom above the hull, and E_g is the normalized absolute deviation of the band gap from that of CZTS. Normalization, *i.e.*, $(x - x_{min})/(x_{max} - x_{min})$, is used to bring all values of the performance indicator x into the range [0,1]. For ΔE_f^d, values of 0 and 1 correspond to the $2Cu_{Zn} + Sn_{Zn}$ and polymorph-averaged $2Cu_{Cd} + Ge_{Cd}$ formation energies under Cu-poor conditions for CZTS (0.67 eV) and CCdGSSe (1.54 eV), respectively. For E_{hull}, values of 0 and 1 correspond to 0.073 eV per atom (CZGSSe) and 0 eV per atom above the hull, respectively (see Table S11 in Section S12 of the ESI†). For E_g, values of 0 and 1 correspond to 0.60 eV and 0 eV deviations from the DFT-HSE band gap of CZTS.[143]

black triangle and the axes, *i.e.*, the closed line segments bounded by the origin and the vertices of the black triangle, correspond to the intrinsic stability/instability (energy above the convex hull at 0 K, E_{hull}), the band gap (E_g), and the formation energy of deep-trap inducing $2Cu_X + Y_X$ defect clusters (ΔE_f^d), which directly relate to the synthesizability, V_{oc}, and I_{sc}, respectively. Each axis is normalized as: (1) $\Delta E_f^d = 0 \equiv 0.67$ eV (taken from CZTS under Cu-poor conditions) and $= 1 \equiv 1.54$ eV (average of stannite- and wurtzite-CCdGSSe); (2) $E_{hull} = 0 \equiv 0.073$ eV per atom (from CZGSSe) and $1 \equiv 0$ eV per atom; and (3) E_g of 0 and 1 correspond to 0.60 eV and 0 eV deviations from the E_g^{HSE} of CZTS, where we plot the DFT-HSE band gaps for CZTS,[143] CZGS,[152] and CCdGSSe (this work), and an experimental gap for CZGSSe.[134] Fig. 7 shows that the performance of CZTS (roughly the area of the green triangle) comes from its stability ($E_{hull} = 0$ eV per atom) and optimal band gap ($E_g^{HSE} = 1.49$ eV (ref. 143) $\approx E_g^{SQ}$). However, CZTS is limited by the ease with which I_{sc}-reducing $2Cu_{Zn} + Sn_{Zn}$ defect clusters form ($\Delta E_f^d = 0.67$ eV). Complete Ge-substitution (CZGS, red), on the other hand, suppresses the formation of these detrimental defects ($\Delta E_f^d = 0.92$ eV), leading to a performance increase along the ΔE_f^d axis, but widens the band gap ($E_g^{HSE} = 2.09$ eV (ref. 152)) too far beyond that of the nearly optimal CZTS value. Partial

selenization (CZGSSe, blue) can be used to improve the band gap (E_g^{exp} = 1.65 eV (ref. 134)) but it also reduces both the Ge-induced suppression of deep defects (ΔE_f^d = 0.77 eV) and the intrinsic stability of the material (E_{hull} = 0.073 eV per atom, ≈2.8 × k_BT at 298 K). Remarkably, complete Cd-substitution (CCdGSSe, magenta) practically eliminates I_{sc}-decreasing 2+/4+ disorder (ΔE_f^d = 1.54 eV), optimizes the band gap (E_g = 1.45 eV), and effectively stabilizes the material (E_{hull} = 0.005 eV per atom < k_BT at 298 K, which is likely thermally accessible).

The stability of CCdGSSe is supported by reports of the synthesis and characterization of the closely related compounds Cu_2CdGeS_4 (ref. 107) and $Cu_2CdGeSe_4$,[108,153–155] which differ from CCdGSSe only in S–Se ratio. For both compounds, we predict E_{hull} = 0 eV per atom, which is consistent with their synthesizability (see Table S11 in Section S12 of the ESI†). Additionally, we predict that CCdGS and CCdGSe prefer the wurtzite and stannite polymorphs, respectively [see Fig. 6c], which agrees with X-ray diffraction measurements.[107,108,153–155] The excellent agreement between theory and experiment for these very closely related compounds CCdGS and CCdGSe suggests that our prediction of the bulk stability of CCdGSSe should be reliable.

We also calculated the thermodynamics of CCdGSSe phase separation, *i.e.*, $Cu_2CdGeS_3Se \rightarrow 3/4Cu_2CdGeS_4 + 1/4Cu_2CdGeSe_4$, and Fig. S1 in Section S2 of the ESI† shows that the configurational entropy of ideal S/Se mixing on the anion sublattice stabilizes CCdGSSe at temperatures above 133 K. Note that the 0 K convex hull at the composition of Cu_2CdGeS_3Se actually consists of Cu_2GeS_3 + CdSe and not the mixture of wurtzite-Cu_2CdGeS_4 and stannite-$Cu_2CdGeSe_4$. We find that the S/Se mixing entropy and vibrational entropic contributions stabilize CCdGSSe with respect to the decomposition into Cu_2GeS_3 + CdSe at temperatures above 879 K (see Fig. S2 and S3 and Table S4 in Section S2 of the ESI†), which is comparable with typical sulfurization temperatures of CZTS and CCdTS, *i.e.*, 580–600 °C or 853–873 K.[77]

The calculated band gap of CCdGSSe (1.45 eV) is bounded by the measured band gaps of CCdGS (1.85–2.05 eV)[118,156–158] and CCdGSe (1.14–1.27 eV)[138,159–161] (see Table S12 in Section S13 of the ESI†), which suggests that our prediction of the optimality of the band gap of CCdGSSe is accurate. Since the measured band gaps of quinary metal sulfide-selenides are proportional to x_{Se},[140,162] that of CCdGSSe should be approximately 1.67–1.86 eV, as found by linear interpolation. While this is slightly greater than the nearly ideal band gap of CZTS (1.49 eV (ref. 143)), further selenization to $Cu_2CdGeS_2Se_2$ (x_{Se} = 0.5) optimizes the interpolated band gap (1.50–1.66 eV) and does not influence our conclusion that complete Cd- and Ge-substitution strongly suppresses the formation of detrimental defects (see Table S13 in Section S13 of the ESI†).

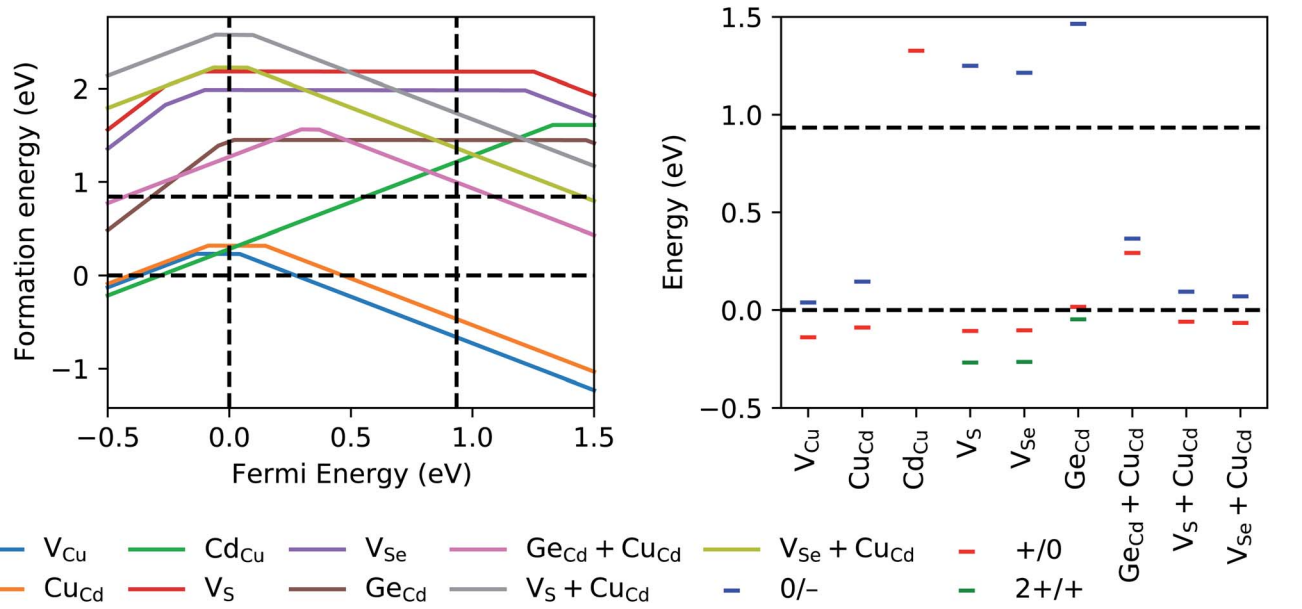

Fig. 8 (Left) GGA+*U*+D formation energies under Cu-poor conditions (*i.e.*, when CCdGS, Cd_4GeS_6, GeS_2, S, and Se are in equilibrium) of various charged vacancies, antisites, vacancy-antisite clusters, and antisite clusters considered within stannite CCdGSSe, plotted as a function of the Fermi energy. Vertical, dashed, black lines at 0 eV and 0.93 eV indicate the GGA+*U*+D VBM and CBM, respectively, where the zero of the Fermi energy is arbitrarily set to the VBM. For V_{Cu}, Cu_{Cd}, Cd_{Cu}, $Ge_{Cd} + Cu_{Cd}$, $V_S + Cu_{Cd}$, and $V_{Se} + Cu_{Cd}$, three ionized states are considered, namely, q = −1 (negatively charged, slope of −1), q = 0 (neutral, zero slope), and q = 1 (positively charged, slope of 1). For V_S, V_{Se}, and Ge_{Cd}, we also consider q = 2 (doubly positively charged, slope of 2). The solid lines indicate the minimum formation energy at each Fermi energy, indicative of the most stable charged state of the defect. Horizontal, dashed, black lines at 0 eV and 0.84 eV respectively indicate the threshold for exothermic defect formation and the GGA+*U*+D formation energy of the neutral $2Cu_{Zn} + Sn_{Zn}$ antisite cluster,[104] which causes Shockley–Read–Hall recombination in CZTS.[41,53,54] The latter constitutes an upper bound on the formation energy of defects that affect solar cell parameters. (Right) Transition levels of the defects in left panel. Blue, red, and green dashes respectively signify acceptor (q, 0 → −1), donor (q, 1 → 0), and donor (q, 2 → 1) transition levels.

It also is crucial to know, for a given Fermi level, the most stable charge state and deep/shallow character of the defect and its potential trapping ability. We therefore calculated the formation energies of the following charged defects and defect clusters in stannite CCdGSSe, which are consistent with those considered in ref. 58: V_{Cu}, Cu_{Cd}, Cd_{Cu}, V_S, V_{Se}, Ge_{Cd}, $V_S + Cu_{Cd}$, and $V_{Se} + Cu_{Cd}$. The left panel of Fig. 8 shows that only V_{Cu} ($q = -1, 0$), Cu_{Cd} ($q = -1, 0$), and Cd_{Cu} ($q = 1$) should form in appreciable quantities for Fermi energies between the valence-band maximum (VBM) and conduction-band minimum (CBM), and under Cu-poor conditions (*i.e.*, when CCdGS, Cd_4GeS_6, GeS_2, S, and Se are in equilibrium). The defect transition levels in the right panel of Fig. 8 agree qualitatively with those for CZTSe, CZTS, CZGSe, and $Ag_2ZnSnSe_4$ in ref. 58, with the exception of Ge_{Cd}, which exhibits deep donor levels within the valence band. The formation energy of Ge_{Cd} (1.44–1.45 eV), however, is well above that of the neutral $2Cu_{Zn} + Sn_{Zn}$ antisite cluster in CZTS (0.84 eV),[104] which constitutes an upper bound on the formation energy of defects that affect solar cell parameters. $Ge_{Cd} + Cu_{Cd}$ also has deep donor and acceptor levels, however, we discard this defect as well because of its high formation energy. Therefore, CCdGSSe should exhibit lower non-radiative recombination than CZTS.

The acceptor transition levels of V_{Cu} and Cu_{Cd} at $E_F - E_{VBM} =$ 39 meV and 146 meV, respectively, agree quantitatively with those in ref. 118, *i.e.*, 27–34 meV and 157 meV, respectively. Therefore, V_{Cu} and Cu_{Cd} likely are present in detectable quantities for CCdGSSe but we expect the absolute Cu_X concentrations to be lower than in CZTS ($\Delta E_f^d = -0.20$ eV for Cu_{Zn} in CZTS *versus* 0.02 eV for Cu_{Cd} in CCdGSSe – see Table S8 in Section S7 in the ESI†). The right panel of Fig. 8 also shows that only Cd_{Cu} has a donor transition level that is close to the conduction band but it is within the band itself. Therefore, we cannot assign the defects and/or defect complexes we considered to the experimentally observed deep donor transition levels at ~50–120 meV below the CBM.[118]

In addition to developing a feasible and original ion substitution scheme for optimizing kesterite solar cells, we also clarify the mechanisms of defect suppression and promotion by Ge and Se, emphasizing the crucial role of the inert pair effect and metal-chalcogen bond covalency, respectively. These insights reveal three important materials design considerations for tuning defect formation in kesterite-type absorbers *via* ion substitution: (1) bond order (BO) conservation, (2) cation redox inactivity, and (3) anion polarizability. The BO conservation principle states that the sum of the strengths of the bonds to an anion from its adjacent cations is nearly equal to its valence.[163] In other words, if some of the anion–cation bonds become stronger, *e.g.*, upon cation substitution, then the others must become weaker in order to conserve the BO of the anion. Such bond strength reciprocity can be used, for example, to tune the formation energy of V_{oc}-increasing Cu vacancies. By replacing Sn with an element that forms stronger bonds with S, such as Ge (BDE = 5.54 ± 0.03 eV for Ge–S *vs.* 4.84 eV for Sn–S),[132] BO conservation dictates that the Cu–S bonds must become weaker; therefore, Cu vacancies should form more easily in CZGS than CZTS, as is shown in Fig. 4b ($\Delta E_f^d = -0.02$ eV for CZGS *vs.* 0.17 eV for CZTS). This same principle is illustrated upon examination of how the formation energies of neutral chalcogen vacancies and their neutral clusters with Cu_X antisites, which also have been predicted theoretically to be strong electron traps,[164] change with X and Y. Table S14 in Section S14 of the ESI† shows that generally Cd (Ge) decreases (increases) the formation energies of these defects compared to Zn (Sn). The effect of compositional changes on the formation energies of these defects again can be rationalized on the basis of 298 K neutral diatomic bond dissociation enthalpies (BDEs): Cd–S bonds (2.16 ± 0.22 eV) are weaker than Zn–S bonds (2.33 ± 0.13 eV) and Ge–S bonds (5.53 eV) are stronger than Sn–S (4.84 eV). Note that uncertainties in the Ge–S and Sn–S BDEs are unavailable.[132]

To illustrate the effect of cation redox activity on defect formation, consider the $2Cu_{Zn} + Sn_{Zn}$ antisite cluster. While Zn exhibits only one normal oxidation state (2+), Cu and Sn exhibit two (1+ and 2+ for Cu and 2+ and 4+ for Sn), where Sn^{2+} is stabilized by the inert pair effect. The redox activities of Cu and Sn promote the formation of Cu_{Zn} and Sn_{Zn} antisites, respectively, because they both can adopt the 2+ oxidation state of Zn, thereby reducing the electrostatic energy penalty associated with the formation of these antisites and, consequently, their clusters. Replacing Sn (2+ and 4+) with an element that is redox inactive, such as Ge (4+), should suppress the formation of I_{sc}-reducing Zn/4+ disorder, as is shown in Fig. 4b ($\Delta E_f^d = 0.92$ eV for CZGS *vs.* 0.67 eV for CZTS).

A final point to consider when designing kesterite solar cell materials is the polarizability of the anion. To explain its significance, we again consider the recombination-inducing $2Cu_{Zn} + Y_{Zn}$ antisite cluster, now focusing on the case where Y = Ge. Despite the fact that this defect is neutral and globally charge compensated (*i.e.*, $2Cu_{Zn}$ and Ge_{Zn} produce two holes and two electrons, respectively, which cancel each other out), the generated charge carriers are, to some extent, delocalized.[104] Since Ge^{4+} is resistant to reduction, with reduction being a likely consequence of localized electrons, the stability of this particular defect depends on the anion's tolerance for delocalization, which can be measured in terms of its polarizability. Given that Se (3.89×10^{-24} cm^3) is more polarizable than S (2.87×10^{-24} cm^3),[132] it should be able to stabilize this detrimental defect, which is precisely what we find in Fig. 5d, where the formation energy of $2Cu_{Zn} + Ge_{Zn}$ decreases almost linearly with increasing x_{Se}.

Based on these considerations, there are a few ion substitution strategies worth exploring further. Note that we, by no means, intend to suggest that the following strategies are exhaustive or the only ones worth pursuing; they are simply those that were inspired by the considerations above. First, while several studies involve Ge- and Se-co-substitution,[121–125,127–131,134,165,166] few vary x_{Ge} and x_{Se} concurrently;[59,136,138] for that reason, there may be room to further improve CZGSSe *via* concurrent and comprehensive variation of x_{Ge} and x_{Se}. Additionally, since we consider only three possible compositions of CCdGSSe and a few, albeit important, defects, opportunities exist for theory to provide a better understanding of its composition-dependent properties and experiments to validate

and augment its performance, *e.g.*, *via* cell fabrication. Another strategy that has proven effective is to replace Cu^+ with redox inactive 1+ cations such as the alkali metal cations[62–72] and Ag^+.[57–61,167] While quaternary and quinary chalcogenides containing these cations have been studied extensively, there remains a great need to explore their post-quinary combinations in conjunction with Ge-, Se-, and Cd-substitution. For example, we suggest Na-doping in either CCdGSSe or CZGSSe (to avoid Cd) as a promising pathway to further mitigate the formation of disorder-causing and V_{oc}-reducing antisites and improve the performance of kesterite-based solar cells.

Conclusions

This work introduces the new photovoltaic material CCdGSSe, which we predict to be nearly thermodynamically stable, have an ideal band gap, and offer substantial suppression of the defects that plague the efficiency of other Cu_2ZnSnS_4-based materials, based on extensive DFT-based calculations. Additionally, we ascribe mechanisms to the dependence of key, performance-affecting defect formation energies on Ge and Se content, revealing how: (1) bond order conservation can be used to tune vacancy formation energies (*e.g.*, decrease the formation energy of V_{oc}-increasing Cu vacancies); (2) the inert pair effect of Sn leads to its redox flexibility and thus promotes I_{sc}-reducing Zn/Sn disorder; and (3) the polarizability of Se stabilizes the local charge imbalances created by cation disorder, thereby reducing the thermodynamic barrier for defect cluster formation. These insights and the materials design principles gleaned in this work should provide the community of CZTS researchers with a heightened intuition for how to optimize kesterite solar cell materials, hopefully enabling this promising photovoltaic technology to reach its full potential.

Conflicts of interest

There are no conflicts to declare.

Acknowledgements

E. A. C. thanks the U.S. Department of Energy, Office of Science, Basic Energy Sciences, under Grant DE-SC0002120 for funding this project. The authors thank Princeton Research Computing resources at Princeton University, a consortium of groups including the Princeton Institute for Computational Science and Engineering and the Princeton University Office of Information Technology's Research Computing department.

Notes and references

1 J. Jean, P. R. Brown, R. L. Jaffe, T. Buonassisi and V. Bulović, *Energy Environ. Sci.*, 2015, **8**, 1200–1219.
2 F. Haase, C. Hollemann, S. Schäfer, A. Merkle, M. Rienäcker, J. Krügener, R. Brendel and R. Peibst, *Sol. Energy Mater. Sol. Cells*, 2018, **186**, 184–193.
3 K. Yoshikawa, H. Kawasaki, W. Yoshida, T. Irie, K. Konishi, K. Nakano, T. Uto, D. Adachi, M. Kanematsu, H. Uzu and K. Yamamoto, *Nat. Energy*, 2017, **2**, 17032.
4 C. Battaglia, A. Cuevas and S. De Wolf, *Energy Environ. Sci.*, 2016, **9**, 1552–1576.
5 K. Peng, Y. Xu, Y. Wu, Y. Yan, S.-T. Lee and J. Zhu, *Small*, 2005, **1**, 1062–1067.
6 S. G. Kumar and K. S. R. K. Rao, *Energy Environ. Sci.*, 2014, **7**, 45–102.
7 X. Wu, *Sol. Energy*, 2004, **77**, 803–814.
8 J. Ma and S.-H. Wei, *Phys. Rev. Lett.*, 2013, **110**, 235901.
9 M. Nakamura, K. Yamaguchi, Y. Kimoto, Y. Yasaki, T. Kato and H. Sugimoto, *IEEE Journal of Photovoltaics*, 2019, **9**, 1863–1867.
10 J. Ramanujam and U. P. Singh, *Energy Environ. Sci.*, 2017, **10**, 1306–1319.
11 S. Siebentritt, M. Igalson, C. Persson and S. Lany, *Prog. Photovoltaics*, 2010, **18**, 390–410.
12 B. M. Kayes, H. Nie, R. Twist, S. G. Spruytte, F. Reinhardt, I. C. Kizilyalli and G. S. Higashi, in *2011 37th IEEE Photovoltaic Specialists Conference*, IEEE, 2011, pp. 000004–000008.
13 P. Dutta, M. Rathi, D. Khatiwada, S. Sun, Y. Yao, B. Yu, S. Reed, M. Kacharia, J. Martinez, A. P. Litvinchuk, Z. Pasala, S. Pouladi, B. Eslami, J.-H. Ryou, H. Ghasemi, P. Ahrenkiel, S. Hubbard and V. Selvamanickam, *Energy Environ. Sci.*, 2019, **12**, 756–766.
14 A. J. Ritenour, J. W. Boucher, R. DeLancey, A. L. Greenaway, S. Aloni and S. W. Boettcher, *Energy Environ. Sci.*, 2015, **8**, 278–285.
15 S. D. Stranks, G. E. Eperon, G. Grancini, C. Menelaou, M. J. P. Alcocer, T. Leijtens, L. M. Herz, A. Petrozza and H. J. Snaith, *Science*, 2013, **342**, 341–344.
16 M. Saliba, T. Matsui, J.-Y. Seo, K. Domanski, J.-P. Correa-Baena, M. K. Nazeeruddin, S. M. Zakeeruddin, W. Tress, A. Abate, A. Hagfeldt and M. Grätzel, *Energy Environ. Sci.*, 2016, **9**, 1989–1997.
17 W.-J. Yin, J.-H. Yang, J. Kang, Y. Yan and S.-H. Wei, *J. Mater. Chem. A*, 2015, **3**, 8926–8942.
18 H.-L. Yip and A. K. Y. Jen, *Energy Environ. Sci.*, 2012, **5**, 5994.
19 Y. Li, *Acc. Chem. Res.*, 2012, **45**, 723–733.
20 Y. Lin, J. Wang, Z.-G. Zhang, H. Bai, Y. Li, D. Zhu and X. Zhan, *Adv. Mater.*, 2015, **27**, 1170–1174.
21 B. O'Regan and M. Grätzel, *Nature*, 1991, **353**, 737–740.
22 Z. Ning, Y. Fu and H. Tian, *Energy Environ. Sci.*, 2010, **3**, 1170.
23 A. Hagfeldt, G. Boschloo, L. Sun, L. Kloo and H. Pettersson, *Chem. Rev.*, 2010, **110**, 6595–6663.
24 L. Ye, Y. Xiong, Q. Zhang, S. Li, C. Wang, Z. Jiang, J. Hou, W. You and H. Ade, *Adv. Mater.*, 2018, **30**, 1705485.
25 W. Zhao, Y. Zhang, S. Zhang, S. Li, C. He and J. Hou, *J. Mater. Chem. C*, 2019, **7**, 3206–3211.
26 A. Kakekhani, R. N. Katti and A. M. Rappe, *APL Mater.*, 2019, **7**, 041112.
27 S. K. Wallace, J. M. Frost and A. Walsh, *J. Mater. Chem. A*, 2019, **7**, 312–321.

28 F. Ye, H. Wu, M. Qin, S. Yang, G. Niu, X. Lu, J. Wang, D. B. Mitzi and W. C. H. Choy, *ACS Appl. Mater. Interfaces*, 2020, **12**, 24498–24504.
29 S. Delbos, *EPJ Photovoltaics*, 2012, **3**, 35004.
30 H. Azimi, Y. Hou and C. J. Brabec, *Energy Environ. Sci.*, 2014, **7**, 1829–1849.
31 H. Zhou, H.-S. Duan, W. Yang, Q. Chen, C.-J. Hsu, W.-C. Hsu, C.-C. Chen and Y. Yang, *Energy Environ. Sci.*, 2014, **7**, 998.
32 H. Zhou, W. C. Hsu, H. S. Duan, B. Bob, W. Yang, T. Bin Song, C. J. Hsu and Y. Yang, *Energy Environ. Sci.*, 2013, **6**, 2822–2838.
33 K. Woo, Y. Kim and J. Moon, *Energy Environ. Sci.*, 2012, **5**, 5340–5345.
34 A. Redinger, D. M. Berg, P. J. Dale and S. Siebentritt, *J. Am. Chem. Soc.*, 2011, **133**, 3320–3323.
35 G. Wang, W. Zhao, Y. Cui, Q. Tian, S. Gao, L. Huang and D. Pan, *ACS Appl. Mater. Interfaces*, 2013, **5**, 10042–10047.
36 K. Yu and E. A. Carter, *Chem. Mater.*, 2016, **28**, 864–869.
37 J. J. Scragg, T. Ericson, T. Kubart, M. Edoff and C. Platzer-Björkman, *Chem. Mater.*, 2011, **23**, 4625–4633.
38 W. Shockley and W. T. Read, *Phys. Rev.*, 1952, **87**, 835–842.
39 R. N. Hall, *Phys. Rev.*, 1952, **87**, 387.
40 K. Yu and E. A. Carter, *Chem. Mater.*, 2015, **27**, 2920–2927.
41 S. Chen, J. H. Yang, X. G. Gong, A. Walsh and S. H. Wei, *Phys. Rev. B: Condens. Matter Mater. Phys.*, 2010, **81**, 35–37.
42 W. Shockley and H. J. Queisser, *J. Appl. Phys.*, 1961, **32**, 510–519.
43 S. Rühle, *Sol. Energy*, 2016, **130**, 139–147.
44 J. J. S. Scragg, L. Choubrac, A. Lafond, T. Ericson and C. Platzer-Björkman, *Appl. Phys. Lett.*, 2014, **104**, 041911.
45 S. Schorr, *Sol. Energy Mater. Sol. Cells*, 2011, **95**, 1482–1488.
46 B. G. Mendis, M. D. Shannon, M. C. Goodman, J. D. Major, R. Claridge, D. P. Halliday and K. Durose, *Prog. Photovoltaics*, 2014, **22**, 24–34.
47 D. P. Halliday, R. Claridge, M. C. J. Goodman, B. G. Mendis, K. Durose and J. D. Major, *J. Appl. Phys.*, 2013, **113**, 223503.
48 G. Rey, A. Redinger, J. Sendler, T. P. Weiss, M. Thevenin, M. Guennou, B. El Adib and S. Siebentritt, *Appl. Phys. Lett.*, 2014, **105**, 112106.
49 J. J. S. S. Scragg, J. K. Larsen, M. Kumar, C. Persson, J. Sendler, S. Siebentritt and C. Platzer Björkman, *Phys. Status Solidi*, 2016, **253**, 247–254.
50 S. Chen, A. Walsh, X.-G. Gong and S.-H. Wei, *Adv. Mater.*, 2013, **25**, 1522–1539.
51 K. Yu and E. A. Carter, *Chem. Mater.*, 2016, **28**, 4415–4420.
52 A. Redinger, D. M. Berg, P. J. Dale, N. Valle and S. Siebentritt, in *2011 37th IEEE Photovoltaic Specialists Conference*, IEEE, 2011, pp. 000025–000025.
53 S. Chen, L. W. Wang, A. Walsh, X. G. Gong and S. H. Wei, *Appl. Phys. Lett.*, 2012, **101**, 223901.
54 Y. S. Yee, B. Magyari-Köpe, Y. Nishi, S. F. Bent and B. M. Clemens, *Phys. Rev. B: Condens. Matter Mater. Phys.*, 2015, **92**, 195201.
55 C. Frisk, T. Ericson, S.-Y. Li, P. Szaniawski, J. Olsson and C. Platzer-Björkman, *Sol. Energy Mater. Sol. Cells*, 2016, **144**, 364–370.
56 M. Courel, J. A. Andrade-Arvizu and O. Vigil-Galán, *Mater. Res. Express*, 2016, **3**, 095501.
57 G. Sai Gautam, T. P. Senftle and E. A. Carter, *Chem. Mater.*, 2018, **30**, 4543–4555.
58 S. Kim, J. A. Márquez Prieto, T. Unold and A. Walsh, *Energy Environ. Sci.*, 2020, 1–11.
59 P. Mangelis, A. Aziz, I. da Silva, R. Grau-Crespo, P. Vaqueiro and A. V Powell, *Phys. Chem. Chem. Phys.*, 2019, **21**, 19311–19317.
60 C. Ma, H. Guo, K. Zhang, N. Yuan and J. Ding, *Mater. Lett.*, 2017, **186**, 390–393.
61 Z. Xu, Z. Guan, J. Yang and Q. Li, *ACS Appl. Energy Mater.*, 2019, **2**, 2779–2785.
62 Y. T. Hsieh, Q. Han, C. Jiang, T. Bin Song, H. Chen, L. Meng, H. Zhou and Y. Yang, *Adv. Energy Mater.*, 2016, **6**, 1–6.
63 G. Altamura, M. Wang and K. L. Choy, *Sci. Rep.*, 2016, **6**, 1–9.
64 Y. Yang, L. Huang and D. Pan, *ACS Appl. Mater. Interfaces*, 2017, **9**, 23878–23883.
65 H. Xin, S. M. Vorpahl, A. D. Collord, I. L. Braly, A. R. Uhl, B. W. Krueger, D. S. Ginger and H. W. Hillhouse, *Phys. Chem. Chem. Phys.*, 2015, **17**, 23859–23866.
66 Z. Wang, N. Brodusch, R. Gauvin and G. P. Demopoulos, *Nano Energy*, 2018, **53**, 130–134.
67 B. Liu, J. Guo, R. Hao, L. Wang, K. Gu, S. Sun and A. Aierken, *Sol. Energy*, 2020, **201**, 219–226.
68 S. Grini, K. V. Sopiha, N. Ross, X. Liu, T. S. Bjørheim, C. Platzer-Björkman, C. Persson and L. Vines, *Adv. Energy Mater.*, 2019, **9**, 1900740.
69 A. Mondal, C. Scheinert and J. G. Radich, *ACS Appl. Energy Mater.*, 2019, **2**, 250–259.
70 J. Kim, G. Y. Kim, T. T. T. Nguyen, S. Yoon, Y.-K. Kim, S.-Y. Lee, M. Kim, D.-H. Cho, Y.-D. Chung, J.-H. Lee, M.-J. Seong and W. Jo, *Phys. Chem. Chem. Phys.*, 2020, **22**, 7597–7605.
71 W. Xiao, J. N. Wang, X. S. Zhao, J. W. Wang, G. J. Huang, L. Cheng, L. J. Jiang and L. G. Wang, *Sol. Energy*, 2015, **116**, 125–132.
72 S. Berman, G. Sai Gautam and E. A. Carter, *ACS Sustainable Chem. Eng.*, 2019, **7**, 5792–5800.
73 M. Johnson, S. V. Baryshev, E. Thimsen, M. Manno, X. Zhang, I. V. Veryovkin, C. Leighton and E. S. Aydil, *Energy Environ. Sci.*, 2014, **7**, 1931–1938.
74 R. Chen and C. Persson, *J. Appl. Phys.*, 2017, **121**, 203104.
75 L. Weston and C. Stampfl, *Phys. Rev. Mater.*, 2018, **2**, 085407.
76 A. Karabulut, A. Sarilmaz, F. Ozel, İ. Orak and M. A. Şahinkaya, *Curr. Appl. Phys.*, 2020, **20**, 58–64.
77 S. Hadke, S. Levcenko, G. Sai Gautam, C. J. Hages, J. A. Márquez, V. Izquierdo-Roca, E. A. Carter, T. Unold and L. H. Wong, *Adv. Energy Mater.*, 2019, **9**, 1902509.
78 X. Jia, H. Guo, C. Ma, K. Zhang, N. Yuan and J. Ding, *Appl. Phys. Lett.*, 2017, **111**, 1–5.
79 W. Wang, M. T. Winkler, O. Gunawan, T. Gokmen, T. K. Todorov, Y. Zhu and D. B. Mitzi, *Adv. Energy Mater.*, 2014, **4**, 1301465.
80 A. Walsh, S. Chen, S. H. Wei and X. G. Gong, *Adv. Energy Mater.*, 2012, **2**, 400–409.

81 G. Kresse and J. Hafner, *Phys. Rev. B: Condens. Matter Mater. Phys.*, 1993, **47**, 558–561.
82 G. Kresse and J. Hafner, *Phys. Rev. B: Condens. Matter Mater. Phys.*, 1994, **49**, 14251–14269.
83 G. Kresse and J. Furthmüller, *Phys. Rev. B: Condens. Matter Mater. Phys.*, 1996, **54**, 11169–11186.
84 P. E. Blöchl, *Phys. Rev. B: Condens. Matter Mater. Phys.*, 1994, **50**, 17953–17979.
85 G. Kresse and J. Hafner, *J. Phys.: Condens. Matter*, 1994, **6**, 8245–8257.
86 J. Sun, A. Ruzsinszky and J. Perdew, *Phys. Rev. Lett.*, 2015, **115**, 036402.
87 J. Heyd, G. E. Scuseria and M. Ernzerhof, *J. Chem. Phys.*, 2003, **118**, 8207–8215.
88 J. Heyd and G. E. Scuseria, *J. Chem. Phys.*, 2004, **121**, 1187–1192.
89 J. Heyd, G. E. Scuseria and M. Ernzerhof, *J. Chem. Phys.*, 2006, **124**, 219906.
90 A. V. Krukau, O. A. Vydrov, A. F. Izmaylov and G. E. Scuseria, *J. Chem. Phys.*, 2006, **125**, 224106.
91 J. P. Perdew, K. Burke and M. Ernzerhof, *Phys. Rev. Lett.*, 1996, **77**, 3865–3868.
92 N. J. Mosey and E. A. Carter, *Phys. Rev. B: Condens. Matter Mater. Phys.*, 2007, **76**, 155123.
93 N. J. Mosey, P. Liao and E. A. Carter, *J. Chem. Phys.*, 2008, **129**, 014103.
94 K. Yu and E. A. Carter, *J. Chem. Phys.*, 2014, **140**, 121105.
95 S. L. Dudarev, G. A. Botton, S. Y. Savrasov, C. J. Humphreys and A. P. Sutton, *Phys. Rev. B: Condens. Matter Mater. Phys.*, 1998, **57**, 1505–1509.
96 B. G. Janesko, T. M. Henderson and G. E. Scuseria, *Phys. Chem. Chem. Phys.*, 2009, **11**, 443–454.
97 T. M. Henderson, J. Paier and G. E. Scuseria, *Phys. Status Solidi B*, 2011, **248**, 767–774.
98 W. P. Huhn and V. Blum, *Phys. Rev. Mater.*, 2017, **1**, 033803.
99 A. J. Garza and G. E. Scuseria, *J. Phys. Chem. Lett.*, 2016, **7**, 4165–4170.
100 M. J. Lucero, T. M. Henderson and G. E. Scuseria, *J. Phys.: Condens. Matter*, 2012, **24**, 145504.
101 J. Paier, M. Marsman, K. Hummer, G. Kresse, I. C. Gerber and J. G. Ángyán, *J. Chem. Phys.*, 2006, **124**, 154709.
102 M. Marsman, J. Paier, A. Stroppa and G. Kresse, *J. Phys.: Condens. Matter*, 2008, **20**, 064201.
103 A. Jain, S. P. Ong, G. Hautier, W. Chen, W. D. Richards, S. Dacek, S. Cholia, D. Gunter, D. Skinner, G. Ceder and K. A. Persson, *APL Mater.*, 2013, **1**, 011002.
104 R. B. Wexler, G. Sai Gautam and E. A. Carter, *Phys. Rev. B: Condens. Matter Mater. Phys.*, 2020, **102**, 054101.
105 S. P. Ong, W. D. Richards, A. Jain, G. Hautier, M. Kocher, S. Cholia, D. Gunter, V. L. Chevrier, K. A. Persson and G. Ceder, *Comput. Mater. Sci.*, 2013, **68**, 314–319.
106 A. Togo and I. Tanaka, *Spglib: a software library for crystal symmetry search*, 2018, pp. 1–11, https://arxiv.org/abs/1808.01590 (written at version 1.10.4).
107 E. Parthé, K. Yvon and R. H. Deitch, *Acta Crystallogr., Sect. B: Struct. Crystallogr. Cryst. Chem.*, 1969, **25**, 1164–1174.
108 L. D. Gulay, Y. E. Romanyuk and O. V. Parasyuk, *J. Alloys Compd.*, 2002, **347**, 193–197.
109 J. W. Lekse, B. M. Leverett, C. H. Lake and J. A. Aitken, *J. Solid State Chem.*, 2008, **181**, 3217–3222.
110 M. Pandey and K. W. Jacobsen, *Phys. Rev. Mater.*, 2018, **2**, 105402.
111 X. Wang, J. Li, Z. Zhao, S. Huang and W. Xie, *J. Appl. Phys.*, 2012, **112**, 023701.
112 J. He, Y. Guo, W. Huang, X. Zhang, J. Yao, T. Zhai and F. Huang, *Inorg. Chem.*, 2018, **57**, 9918–9924.
113 A. Babayigit, A. Ethirajan, M. Muller and B. Conings, *Nat. Mater.*, 2016, **15**, 247–251.
114 S. Ikegami, *Sol. Cells*, 1988, **23**, 89–105.
115 S. P. Albright, J. F. Jordan, B. Ackerman and R. R. Chamberlin, *Sol. Cells*, 1989, **27**, 77–90.
116 S. D. Hodgson, W. S. M. Brooks, A. J. Clayton, G. Kartopu, V. Barrioz and S. J. C. Irvine, *Nano Energy*, 2013, **2**, 21–27.
117 G. Bergerhoff and I. D. Brown, *Acta Crystallogr., Sect. A: Found. Crystallogr.*, 1981, **37**, C342.
118 J. Krustok, T. Raadik, X. Li, M. Kauk-Kuusik, K. Timmo, S. Oueslati and M. Grossberg, *J. Phys. D: Appl. Phys.*, 2020, **53**, 275102.
119 Y. Kumagai and F. Oba, *Phys. Rev. B: Condens. Matter Mater. Phys.*, 2014, **89**, 195205.
120 M. Arrigoni and G. K. H. Madsen, *The Spinney package*, https://spinney.readthedocs.io/en/latest/, accessed 8 February 2021.
121 N. Saini, J. K. Larsen, K. V. Sopiha, J. Keller, N. Ross and C. Platzer Björkman, *Phys. Status Solidi*, 2019, **216**, pssa.201900492.
122 S. Nakamura, T. Maeda and T. Wada, *Jpn. J. Appl. Phys.*, 2010, **49**, 121203.
123 D. B. Khadka, S. Kim and J. Kim, *J. Phys. Chem. C*, 2016, **120**, 4251–4258.
124 M. Neuschitzer, J. Marquez, S. Giraldo, M. Dimitrievska, M. Placidi, I. Forbes, V. Izquierdo-Roca, A. Pérez-Rodriguez and E. Saucedo, *J. Phys. Chem. C*, 2016, **120**, 9661–9670.
125 S. Giraldo, E. Saucedo, M. Neuschitzer, F. Oliva, M. Placidi, X. Alcobé, V. Izquierdo-Roca, S. Kim, H. Tampo, H. Shibata, A. Pérez-Rodríguez and P. Pistor, *Energy Environ. Sci.*, 2018, **11**, 582–593.
126 A. F. Moodie and H. J. Whitfield, *Acta Crystallogr.*, 1986, **B42**, 236–247.
127 S. Niedenzu, G. Gurieva and S. Schorr, *Thin Solid Films*, 2019, **669**, 625–628.
128 S. Bag, O. Gunawan, T. Gokmen, Y. Zhu and D. B. Mitzi, *Chem. Mater.*, 2012, **24**, 4588–4593.
129 I. Kim, K. Kim, Y. Oh, K. Woo, G. Cao, S. Jeong and J. Moon, *Chem. Mater.*, 2014, **26**, 3957–3965.
130 C. J. Hages, S. Levcenco, C. K. Miskin, J. H. Alsmeier, D. Abou-Ras, R. G. Wilks, M. Bär, T. Unold and R. Agrawal, *Prog. Photovoltaics*, 2015, **23**, 376–384.
131 A. D. Collord and H. W. Hillhouse, *Chem. Mater.*, 2016, **28**, 2067–2073.
132 *CRC Handbook of Chemistry and Physics*, ed. J. R. Rumble, CRC Press, Taylor & Francis Group, 100th edn, 2019.

133 O. Kubaschewski and C. B. Alcock, *Metallurgical Thermochemistry*, Pergamon Press, 5th edn, 1959, vol. 12.
134 C. P. Heinrich, T. W. Day, W. G. Zeier, G. J. Snyder and W. Tremel, *J. Am. Chem. Soc.*, 2014, **136**, 442–448.
135 D. Chen and N. M. Ravindra, *J. Alloys Compd.*, 2013, **579**, 468–472.
136 D. B. Khadka and J. Kim, *J. Phys. Chem. C*, 2015, **119**, 1706–1713.
137 Q. Yi, J. Wu, J. Zhao, H. Wang, J. Hu, X. Dai and G. Zou, *ACS Appl. Mater. Interfaces*, 2017, **9**, 1602–1608.
138 H. Matsushita, T. Ichikawa and A. Katsui, *J. Mater. Sci.*, 2005, **40**, 2003–2005.
139 S. Chen, X. G. Gong, A. Walsh and S.-H. Wei, *Appl. Phys. Lett.*, 2009, **94**, 041903.
140 S. Ahn, S. Jung, J. Gwak, A. Cho, K. Shin, K. Yoon, D. Park, H. Cheong and J. H. Yun, *Appl. Phys. Lett.*, 2010, **97**, 021905.
141 L. Pauling, *J. Am. Chem. Soc.*, 1932, **54**, 3570–3582.
142 A. L. Allred, *J. Inorg. Nucl. Chem.*, 1961, **17**, 215–221.
143 J. Paier, R. Asahi, A. Nagoya and G. Kresse, *Phys. Rev. B: Condens. Matter Mater. Phys.*, 2009, **79**, 1–8.
144 N. Sarmadian, R. Saniz, B. Partoens and D. Lamoen, *J. Appl. Phys.*, 2016, **120**, 085707.
145 A. Crovetto, M. L. N. Palsgaard, T. Gunst, T. Markussen, K. Stokbro, M. Brandbyge and O. Hansen, *Appl. Phys. Lett.*, 2017, **110**, 083903.
146 H. J. Gu, J.-H. Yang, S. Y. Chen, H. J. Xiang and X. G. Gong, *APL Mater.*, 2019, **7**, 091104.
147 S. N. Hood, A. Walsh, C. Persson, K. Iordanidou, D. Huang, M. Kumar, Z. Jehl, M. Courel, J. Lauwaert and S. Lee, *JPhys Energy*, 2019, **1**, 042004.
148 W. Xiao, J. N. Wang, J. W. Wang, G. J. Huang, L. Cheng, L. J. Jiang and L. G. Wang, *Phys. Chem. Chem. Phys.*, 2016, **18**, 12029–12034.
149 R. D. Shannon, *Acta Crystallogr., Sect. A: Cryst. Phys., Diffr., Theor. Gen. Crystallogr.*, 1976, **32**, 751–767.
150 M. A. Green, E. D. Dunlop, J. Hohl-Ebinger, M. Yoshita, N. Kopidakis and A. W. Y. Ho-Baillie, *Prog. Photovoltaics*, 2020, **28**, 3–15.
151 E. H. Jung, N. J. Jeon, E. Y. Park, C. S. Moon, T. J. Shin, T.-Y. Yang, J. H. Noh and J. Seo, *Nature*, 2019, **567**, 511–515.
152 Y. Zhang, X. Sun, P. Zhang, X. Yuan, F. Huang and W. Zhang, *J. Appl. Phys.*, 2012, **111**, 063709.
153 M. G. Brik, O. V. Parasyuk, G. L. Myronchuk and I. V. Kityk, *Mater. Chem. Phys.*, 2014, **147**, 155–161.
154 E. G. Zhukov, S. A. Mkrtchyan, K. Dovletov, A. G. Melikdzhanyan, V. T. Kalinnikov and A. Ashirov, *Russ. J. Inorg. Chem.*, 1984, **29**, 1087–1088.
155 E. G. Zhukov, S. A. Mkrtchyan, K. Dovletov, A. G. Melikdzhanyan, V. T. Kalinnikov and A. Ashirov, *Russ. J. Inorg. Chem.*, 1984, **29**, 1897–1898.
156 G. Y. Davydyuk, O. V. Parasyuk, Y. E. Romanyuk, S. A. Semenyuk, V. I. Zaremba, L. V. Piskach, J. J. Kozioł and V. O. Halka, *J. Alloys Compd.*, 2002, **339**, 40–45.
157 G. E. Davidyuk, O. V. Parasyuk, S. A. Semenyuk and Y. E. Romanyuk, *Inorg. Mater.*, 2003, **39**, 919–923.
158 M. G. Brik, I. V. Kityk, O. V. Parasyuk and G. L. Myronchuk, *J. Phys.: Condens. Matter*, 2013, **25**, 505802.
159 H. Matsushita, T. Maeda, A. Katsui and T. Takizawa, *J. Cryst. Growth*, 2000, **208**, 416–422.
160 M. Kauk-Kuusik, X. Li, M. Pilvet, K. Timmo, M. Grossberg, T. Raadik, M. Danilson, V. Mikli, M. Altosaar, J. Krustok and J. Raudoja, *Thin Solid Films*, 2018, **666**, 15–19.
161 J. Krustok, T. Raadik, R. Kaupmees, M. Grossberg, M. Kauk-Kuusik, K. Timmo and A. Mere, *J. Phys. D: Appl. Phys.*, 2019, **52**, 285102.
162 M. Singh, T. R. Rana and J. H. Kim, *J. Alloys Compd.*, 2016, **675**, 370–376.
163 L. Pauling, *The Nature of the Chemical Bond and the Structure of Molecules and Crystals: An Introduction to Modern Structural Chemistry*, Cornell University Press, Ithaca, 3rd edn, 1960.
164 S. Kim, J. S. Park and A. Walsh, *ACS Energy Lett.*, 2018, **3**, 496–500.
165 O. V. Parasyuk, L. V. Piskach, Y. E. Romanyuk, I. D. Olekseyuk, V. I. Zaremba and V. I. Pekhnyo, *J. Alloys Compd.*, 2005, **397**, 85–94.
166 G. M. Ford, Q. Guo, R. Agrawal and H. W. Hillhouse, *Chem. Mater.*, 2011, **23**, 2626–2629.
167 C. Wang, S. Chen, J. H. Yang, L. Lang, H. J. Xiang, X. G. Gong, A. Walsh and S. H. Wei, *Chem. Mater.*, 2014, **26**, 3411–3417.
168 United States Environmental Protection Agency, *Radioactive Decay*, https://www.epa.gov/radiation/radioactive-decay, accessed 27 April 2020.
169 The European Parliament and The Council of the European Union, *Off. J. Eur. Communities: Inf. Not.munities: Legis.*, 2011, **54**, 88–110.